



Politecnico di Torino
III Facoltà di Ingegneria

Master thesis

Simulation of InSe for single photon emission application

Master degree in Nanotechnologies for ICTs

Professors: Giancarlo Cicero, Francesca Risplendi

Author: Mattia Salomone

Contents

Acknowledgments	1
Introduction	2
1 Materials and devices for single photon emission	4
1.1 What is Single Photon Emission	4
1.2 Single photon emission devices	5
1.2.1 Application of SPE to quantum computing and simulation	6
1.2.2 Application of SPE in medicine	7
1.3 Materials for SPE	9
1.3.1 State of the art	9
1.3.2 2D semiconductors	11
1.4 InSe as a promising 2D material for SPE	12
1.4.1 InSe Bulk and 2D Structure	12
1.4.2 InSe optical and electronic properties	14
2 Methods	16
2.1 The adiabatic approximation	16
2.2 Density functional theory	17
2.2.1 The Hohenberg-Kohn theorems	18
2.2.2 The Kohn-Sham equations	19
2.2.3 LDA and GGA approximation	20
2.3 The Hellmann-Feynman theorem	21
2.4 Practical aspects of DFT implementation	22
2.4.1 Basis set	22
2.4.2 Pseudopotential theory	23
2.4.3 Reciprocal-space integration and \mathbf{k} points sampling	25
2.5 Cluster Expansion	26
3 Computational approach and accuracy tests	30
3.1 β -InSe	31
3.1.1 PW cutoff energy convergence	31

3.1.2	K-points sampling convergence	32
3.2	2D InSe monolayer	32
3.2.1	Equilibrium structure	32
3.2.2	Band diagram	34
3.2.3	Spin Orbit Coupling effect	36
3.3	Defects in 2D InSe: the supercell approach	38
3.3.1	Selenium vacancy formation energy	39
3.3.2	Selenium vacancy electronic properties	40
4	Study of vacancies and substitutional impurities in InSe monolayer	44
4.1	Se vacancy defect	44
4.2	Group VI substitutional impurities: O and S	46
4.3	Group V substitutional impurities: N, P and As	48
4.4	Group IV substitutional impurities: Ge	49
4.5	Final discussion of impurity defects in InSe	52
5	Properties of $In_{1-x}Ga_xSe$ alloys	56
5.1	$In_{1-x}Ga_xSe$ phase diagram	56
5.2	$In_{1-x}Ga_xSe$ electronic properties	59
	Conclusions	62

Acknowledgments

First of all, I would like to thank Professors Giancarlo Cicero and Francesca Risplendi for their availability, patience and for their guidance. They have always been careful supervisors and this work wouldn't have been possible without them.

Furthermore I'm also grateful to Federico Raffone for his help and his advises.

Finally, I wish to acknowledge my family and all my friends that constantly supported me.

Computational resources were provided by HPC@POLITO, a project of Academic Computing within the Department of Control and Computer Engineering at the Politecnico di Torino (<http://hpc.polito.it>).

Introduction

The importance of photonic technologies is steadily growing in our daily lives. In this field a new frontier of research is the development of non-classical light sources, like, for example, sources that produce streams of photons with controllable quantum correlations. With this respect a central building blocks are single-photon emitters (SPE). Unlike classical light sources, SPEs are fundamental quantum devices for many scalable and leading technologies, such as quantum information and information, precision metrology and imaging. The ability to tailor and control quantum emitters, in order to realize efficient and scalable architectures, depends on site-selective defect engineering. In this work we predicted the electronic properties of an InSe monolayer and its applicability as SPE when impurity defects are introduced in the structure.

InSe is a layered compound consisting of several stacked InSe monolayers; each monolayer is composed by four atoms in the 2D unit cell. The single monolayer structure (2D phase) can be obtained through graphene-like exfoliation processes or by Physical Vapor Deposition (PVD) and it is considered as one of the most promising materials for SPE applications for several reasons. Firstly, 2D InSe has a wide bandgap (around 2.9 eV) which can be tuned through the addition of substitutional impurities, moreover the two-dimensional nature of the monolayer allows for an easy modification of the crystal lattice with respect to bulk materials exploiting, for example, Focused Ion Beam (FIB), Scanning Probe Microscopy (SPM) and Scanning Electron Microscopy (SEM), or through the application of localized strains to the lattice. For these reasons one has the possibility to create SPE in a broad range of energies by employing 2D InSe. In this thesis work, we predict the electronic properties of InSe containing different substitutional impurities by using Density Functional Theory (DFT) simulations. For each system we calculate the formation energies, the band structure and the density of states. The best results to employ InSe as SPE are obtained for As, P, N and Ge substitutional impurities. In the last part of the work InGaSe alloys are studied through the combination of DFT and Cluster Expansion method, and their electronic properties predicted for different In/Ga fractions.

The discussion is organized as follows. The first Chapter provides a general explanation of the single-photon-emission phenomenon and describes two possible applications of this physical process. Materials exploited up to now and aspects that mostly make InSe an outstanding material to be used as SPE are also evidenced. Chapter 2 is centered on

the computational methodology that has been applied to investigate monolayer InSe and the InGaSe alloys, in particular it provides a general description of the Density Functional Theory (DFT) along with the practical aspects related to its implementation, and illustrate the Cluster Expansion method both from a theoretical and from a practical point of view. Chapter 3 reports tests that have been used to determine the optimal computational conditions for the simulations performed in this thesis work. In Chapter 4 the electronic properties of InSe containing different substitutional impurities are reported and discussed in terms of formation energy, band diagram, density of states and spatial distribution of the molecular orbital associated to the lattice modification. In particular we focused our investigation on defect such as selenium vacancy and Ga, Ge, N, P, As, O and S substitutional impurities. Promising results for SPE are obtained for N, P, As and Ge substitutional impurities. In Chapter 5, to conclude, we present the prediction of the structure and electronic properties of InGaSe alloys, obtained through the Cluster Expansion method. Although it comes out that this material is not suitable to be employed directly as single photon emitter, since there are not energy states within its bandgap, its optical emission or absorption can be continuously tuned within a section of the visible spectra by tuning the composition of the alloy and thus it could find applications in many optoelectronic devices.

CHAPTER 1

Materials and devices for single photon emission

1.1 What is Single Photon Emission

An ideal single-photon source, inherently nonclassical in its nature, produces a single photon in a known single mode each and every time one is called for, and that mode must be identical each time [1], [2], [3]. It is distinct from coherent light sources (lasers) and thermal light sources such as incandescent light bulbs [4], [5], [6], [7], [8], [9], [2], [10], [11], [12]. In quantum theory, photons describe quantized electromagnetic radiation. Specifically, photons are elementary excitations of normal modes of the electromagnetic field as solutions to Maxwell's equations [13]. Thus, single photons are single excitations of modes of the electromagnetic field and, therefore, are in the one-photon number state $|1\rangle$ (Fock state) [13]. Photons from an ideal single-photon source exhibit quantum mechanical characteristics. These characteristics include photon antibunching, so that the time between two successive photons is never less than some minimum value [14].

While this ideal source can never be achieved in the real world due to inevitable losses and nonzero multiphoton rates, there have been efforts at making better and better approximations to such an ideal source. The two basic approaches to constructing single-photon sources are based either on the isolated single quantum systems that can only emit one photon at a time or on sources that emit photons in pairs so that the detection of one photon heralds the existence of the second photon.

Figure 1.1 reports the simplest isolated quantum system able to produce this kind of emission: a two level system. A simple scheme of the process is shown: an external source, for example a laser pulse, provides an extra energy to one electron which at first was in its ground state, this $+\Delta E$ is used to promote the electron to an excited state (according to the specific selection rules governing that specific system) resulting in the formation of an electron-hole pair called exciton. The spontaneous decay of a

single exciton (after an average life time τ) leads to the emission of one single photon because the energy states among which the transition occurs do not show a broadening in energies [7]. This means that the two levels involved in the process are characterized by two well defined energies E_1 and E_2 and for this reason the frequency ν associated to the emitted radiation will be given simply by the relation $E_2 - E_1 = h\nu$.

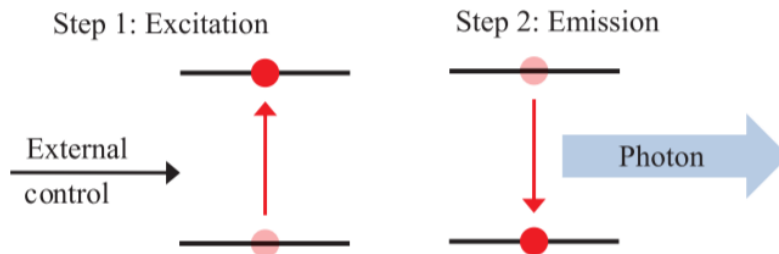


Figure 1.1: Single photon Emission phenomenon in a two-level system (image taken from article [7])

The fundamental component required to create this type of light source is the Single Photon Emitter (SPE) which is basically, at least from a theoretical point of view, an on-demand source (i.e. it can release a light radiation at any arbitrary time defined by the user) able to emit light pulses (the repetition rate must be arbitrarily fast) containing exactly one photon (with the probability of emitting a single photon of 100%) and, furthermore, the produced single photon must be in a known single mode that must be identical each time [15]. One way to assess the quality of the output of a single-photon source is to measure its absolute fidelity to a single photon in a single mode, which may be done by means of the normalized Glauber second-order correlation function $g^{(2)}(0)$ [16]. It quantifies the multiphoton component of the state with respect to the single-photon component (i.e., $|n\rangle$ vs $|1\rangle$). Ideal single-photon sources show $g^{(2)}(0) = 0$ and a realistic single-photon sources must have $g^{(2)}(0)$ tending towards zero. The second-order correlation function can be measured using the Hanbury-Brown-Twiss effect [13], [17], [18].

1.2 Single photon emission devices

The research in the realization and development of new light sources, which produce photons whose statistics and correlations are based on the quantum-mechanical theory, has stimulated interest in the scientific community due to its wide field of possible applications: quantum computing and simulation [19], quantum information [20], sensing [21], nuclear medicine tomographic imaging techniques (such as the so called SPECT, i.e. Single Photon Emission Computed Tomography [22]), and quantum communication [23]. Of course, when one faces to the real world, it is necessarily to take into account the presence of deviations from these ideal characteristics [7], [24]. However,

despite the existence of these non-idealities, promising results and applications are based on the single photon emission theory. In the following, we analyse some state of the art devices published in literature exploiting SPE phenomena.

1.2.1 Application of SPE to quantum computing and simulation

One of the present directions in quantum science is the realization of the so-called *quantum orreries* [19]. They are basically quantum devices that are able to simulate the behaviour of other quantum systems with the advantage, with respect to the exploitation of a general purpose quantum computer, that they are designed to reproduce more complex systems with fewer resources [19]. According to the kind of property they are asked to simulate, there are two types of quantum simulators: the first one mimics collective features such as a quantum phase transition and in this case a global control of the quantum particle is sufficient; the second type, instead, is used to study molecular and atomic systems therefore it requires precise local control and addressability of individual particles.

Quantum simulators of physical systems can be constructed using a variety of quantum architectures, such as atoms [25], [26], [27], [28], ions [29], [30], [31], [32], [33], [34] and single photons. From a practical point of view, in a quantum simulation it is first necessary to choose a suitable mathematical model for the quantum system we want to represent, for example a molecule can be mapped to the non-relativistic Schrödinger equation. Then this model must be executed by a quantum-software layer, which is in turn mapped to a quantum hardware [19], and the molecular eigenvalues associated to the Hamiltonian of the system can be diagonalized by carrying out an iterative phase-estimation algorithm (a *quantum-chemistry algorithm*, [35]) based on a proposal by Abrams and Lloyd [36], [37]: the use of quantum phase estimation to obtain molecular eigenvalues. The simulation should provide a measure of a certain property, however, not all of them are available in short times and in order to obtain a complete map of the wavefunction of the system it may be necessary to perform a large number of measurements which rapidly increases with the number of particles involved [19]. Among all the possible architectures, the photonic quantum system is one of the more promising since the use of single photons leads to a series of important advantages; first of all, single photons can be manipulated and individually addressed with high precision by employing simple optical components, secondly they are easily moved either in free space or in waveguides and their mobility enables them to transmit information at the speed of light. This allows, in principle, the simulation of complex and non-local many-body interactions.

Here is reported an example of simulation, taken from article [38], in which the single photons architecture has been successfully exploited to study quantum aspects of the hydrogen molecule using two entangled photons [19]. A proper time-independent

Hamiltonian \mathcal{H} has been chosen to describe the system and its eigenvalues, i.e. the molecular energies, have been then obtained exploiting a quantum algorithm made of three distinct steps [38], [39]. First of all, the molecular wavefunction have been converted into qubits, each of them, in turn, encoded in the polarization of the single photons (logical $|0\rangle = |H\rangle =$ horizontal polarization and logical $|1\rangle = |V\rangle =$ vertical polarization). After that, its time evolution have been simulated using quantum logic gates (implemented through birefringent wave plates used to perform arbitrary polarization rotations, [38]) and, in the last step, $\hat{\mathcal{H}}$ eigenvalues have been extracted using the already mentioned phase estimation algorithm [39], [40] which is based on the following assumption: considering a molecular eigenstate $|\psi\rangle$ which is under the action of the time-evolution operator $\hat{U} = e^{-(i\hat{H}t/\hbar)}$ [38] one can write the following equation:

$$e^{-(i\hat{H}t/\hbar)}|\psi\rangle = e^{-(iEt/\hbar)}|\psi\rangle = e^{-i2\pi\phi}|\psi\rangle$$

where E is the eigenvalue of the Hamiltonian. The algorithm estimates the phase ϕ accumulated, therefore E can be calculated. In order to perform a measure, two qubits (i.e. two single photons) were required: the polarization of the *register photon* is rotated into a state that represents one eigenstate of $\hat{\mathcal{H}}$, while the *control photon* is rotated into the superposition state $(|H\rangle + |V\rangle)/\sqrt{2}$ (not possible with the classical bit, [41]). Both modes pass through an optical network that implements a controlled \hat{U} -gate and at the end of the path the polarization of the control photon is measured allowing for a phase shift estimation which leads to the possibility to calculate the eigenvalue E.

An example of a possible circuit which exploits the single photons architecture is shown in figure 1.2. It is composed by phase shifter and beam splitter arrays that are used to manipulate the quantum state of light [42].

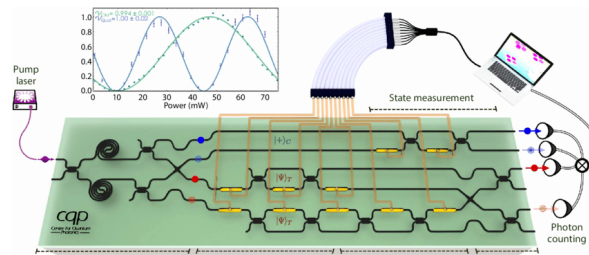


Figure 1.2: Schematic of a quantum circuit composed by beam splitters and phase shifters taken from reference [43]

1.2.2 Application of SPE in medicine

Focusing our attention on the medical applications, the Single-photon emission computed tomography (SPECT) represents a powerful diagnostic tool and a very common

application of SPE. It is a method of computed tomography that uses radionuclides which emit a single photon of a given energy to provide a 3D image of a specific region of the patient [22]. A radionuclide is an unstable atom which can undergo to radioactive decay and in case emit a gamma ray. The radioisotope is delivered into the person, usually through injection into the bloodstream. Most of times, it is attached to a specific ligand to assure binding events only with the tissues of interest. Imaging is then performed by using a gamma camera to acquire multiple 2D images from multiple angles. It is rotated 180 or 360 degrees around the patient to capture images at different positions along the arc [22]. Once the analysis is concluded, the 3D distribution of radionuclides in the anatomic part of interest can be reconstructed through the use of a computer.

The main advantage of this technique is that it can be used to observe biochemical and physiological processes as well as size and volume of the organ [22]; however a big disadvantage is a lower quality of the image with respect to other tomographic methods such as the positron-emission tomography. Since SPECT is sensitive to the level of biological activity at each place in the 3D region analyzed, it can be used to provide information about localised function in internal organs, such as functional cardiac or brain imaging. In picture 1.3, taken from [44], one can see, as an example, the comparison between the biological activity of an healthy brain compared to the one of an individual who abuses alcohol. The Brain SPECT scanning generates three-dimensional images of blood flow in the two tissues allowing for quantitatively analysis.

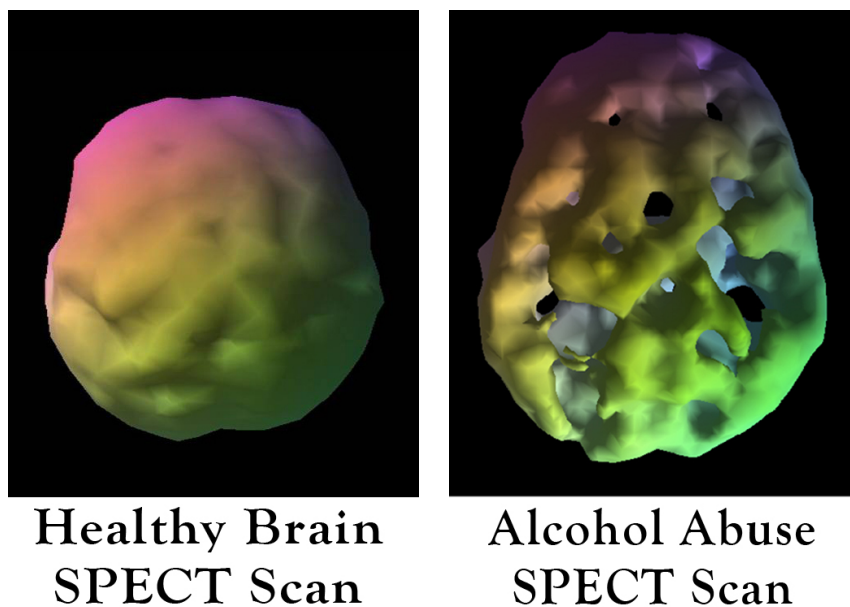


Figure 1.3: Comparison between the images of brains of two persons with different lifestyles obtained via SPECT

1.3 Materials for SPE

In the previous sections we have briefly described the general physical concepts on which the SPE is based and presented some example of its possible applications in many scientific fields. We now present some possible single photon sources reported in the literature.

1.3.1 State of the art

As already said, the ideal SPE is an on-demand, deterministic source able to produce single-photon light pulses in a well defined polarization mode which is identical each time. In nature, systems that are able to produce this kind of radiation are the two-level systems, i.e. single atoms. However, from a technological point of view, it's almost impossible to scale an architecture which deals with single atoms, thus we need something different.

The main idea is to engineer a material in such a way to obtain in its band structure two well defined energy states between which the electronic transitions can take place. In particular, we want to create a flat state within its bandgap because in this way we are able to precisely tune energies of emitted photons (this would be impossible exploiting CB to VB transitions due to the non-flatness of the energy levels involved).

Up to now, single photon sources have been obtained by means of isolated color centers in wide bandgap semiconductors. Colour centers are defects in the regular spacing of atoms of a crystal lattice which are able to absorb light of only specific wavelengths and they have been exploited in many ways: in 3-dimensional and 2-dimensional materials such as diamond (3D) and hexagonal boron nitride h-BN (2D) for instance [45], [46], [47] [48] [49], but also in 1-dimensional materials, such as carbon nanotubes [46] and InP nanowires [50] and 0-dimensional materials, such as GaAs and InGaAs quantum dots [51], [52].

An interesting example is the nitrogen-vacancy (N-V) color center in diamond lattice. It consists of a nearest-neighbor pair of a nitrogen atom, in place of a carbon one, and a lattice vacancy. The absence of a negatively-charged ion from the site it would be attracts and traps an electron [53] which in turn becomes able to absorb only specific colours of light. In figure 1.4 we can see the diamond lattice modification: the charge state $N - V^0$ is neutral, while $N - V^-$ is negative due to the presence of the electron.

Even if the detailed microscopic origin of the quantum emission is still not understood for complex systems such as bulk and 2D materials, highly localized strain gradients associated to the presence of imperfections in the flake (such as edges, wrinkle or nanobubbles in the monolayer, [21], [55]) and the addition to the lattice of vacancies [56], [57] or substitutional impurities [55], [56], [57], [58], [59], [60], [61] are often correlated to the physical origin of single photon emitters [21]. It is plausible to think that

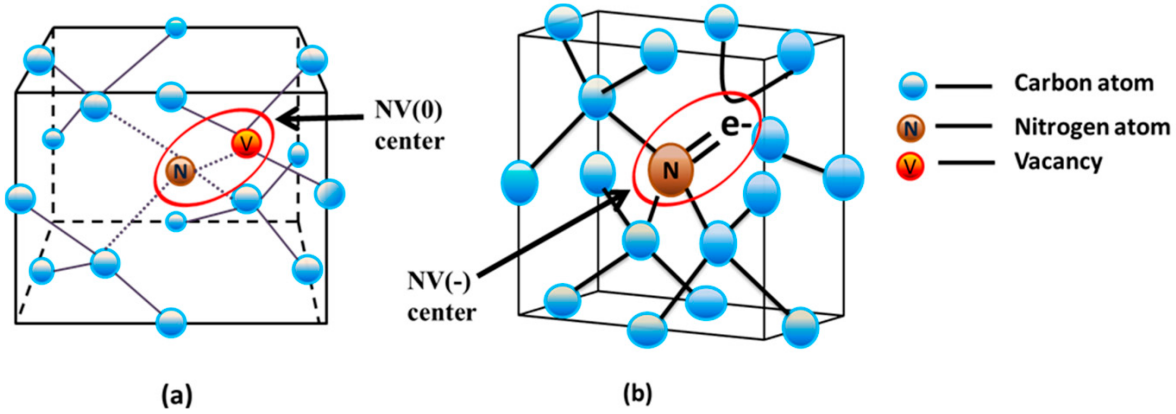


Figure 1.4: Nitrogen-vacancy colour center in its two possible states (neutral on the left) and negative (on the right) [54]

the strain gradient helps to funnel the exciton, while the presence of point defects leads to its localization at the length scale of the exciton Bohr radius (EBR) meaning that the exciton become trapped in a sort of quantum trap [62], [21], [63], [64]. However,

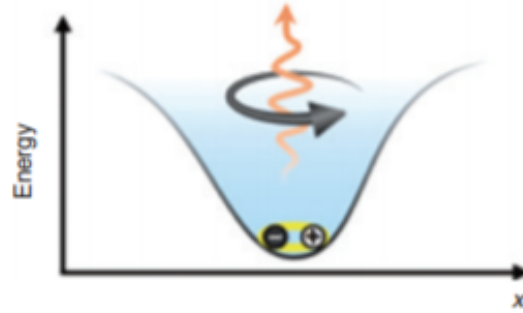


Figure 1.5: Trapped exciton in a strain gradient (image taken from article [21])

it is not sufficient to provide a localized strain or to add a substitutional impurity to guarantee a single photon emission, indeed this phenomenon is observed only in some specific materials which has been previously ad hoc engineered.

In the following paragraph we discuss the main properties that a good SP emitter should have.

To achieving efficient single photon emission, it is mandatory to avoid electron/hole recombination due to thermal effects. To this aim, the energy state arising from the presence of a lattice modification (such as a vacancy or a substitutional defect) must be deep in the semiconductor bandgap. As a consequence, material with a wide energy gap are the most suitable candidates to be used as single photon emitters. Furthermore, a wide tunable bandgap can be also exploited to achieve a full spectral range single photon source (from ultraviolet to near-infrared, the already mentioned h-BN is an example), indeed, by engineering the material with specific substitutional impurities,

one can obtain different defect energy levels within the gap. It is also important to highlight that in order to avoid dispersion in the reciprocal space and to allow, instead, the emission of photons with a well definite wavelength, defect states should not present strong hybridization with the host matrix [65]. The spectral wandering can be also reduced improving the material quality [66] thus material with high chemical and thermal stability are preferable.

1.3.2 2D semiconductors

One should also highlight that, in order to realize efficient and scalable architectures for SPE devices, one has to be able to design emitters with identical properties that can be placed at specific locations on a chip. As a consequence, it is required the capability to deal with atoms and nanostructures with an extremely high precision, i.e. at the atomic scale. This can be particularly difficult for conventional 3D semiconductors, where defects can be buried deep within the bulk structure (think for example to the N-V colour center in diamond), and a possible solution is therefore to exploit two dimensional materials which show many advantages with respect to their 3D counterparts.

Many techniques that allow for manipulation of individual atoms are indeed by far easier to be performed onto a monolayer than onto a bulk structure. For example, Focus Ion Beam (FIB), Scanning Probe Microscopy (SPM) and Scanning Electron Microscopy (SEM), methods that can be used both for imaging and for changing the atomic configuration of a crystal, are more suited for the modification of the top most layers of a material. To modify deeper layers, indeed, higher energies would be required to increase the penetration depth of the beams, but this would imply a higher degree of damage of the substrate which in turns would lead to a wandering of the emission spectrum. Furthermore, in addition their two-dimensional nature which leads to the easier atomic scale manipulation, 2D materials provide a smaller footprint than most conventional solid-state quantum emitters [21] and for this reason they are also easier to integrate with already existing photonic structures.

Obviously, when someone says "2D material", one immediately thinks of graphene. Can the graphene be a good material for the purposes of this work? Graphene owns extremely high carrier mobilities and breaking strength [67], [68], [69] and thank to these qualities it is considered as one of the most promising material for many future applications. However, it does not show an intrinsic bandgap and this lack represents a big obstacle for its applicability in electronics. Indeed, as previously discussed, a bandgap is mandatory for the realization of many devices such as field-effect transistors, functional junctions for optoelectronics based on two-dimensional materials [70] and, above all, for Single Photon Emitters. In order to overcome the limitation of a zero bandgap, many other 2D materials have been taken into account in the last years as possible SPE candidates. MoS_2 , WS_2 , $MoSe_2$, WSe_2 , $MoTe_2$ [71], [72] are the

so called Transition Metal Dichalcogenides (TMDs) and along with their cousins InSe and GaSe (which are instead metal monochalcogenides) represent a family of layered bulk semiconductive materials. Thank to the nature of their chemical bonds, which are strong within the same layer (covalent bonds) and weak between two different layers (Van der Waals forces), it is possible to reduce them into their single-layer phase through graphene-like exfoliation or other processes [70], [71] and for this reason many studies have been focused on them [73]. They exhibit strong light-matter interaction which leads to their large exciton binding energy, linear and nonlinear optical properties and spin-valley coupling [74] which quenches the valley hybridization (i.e. little dispersion of the energy level, [65]). They also possess a wide layer-dependent bandgap and, in addition, the degree of confinement can be engineered through electrostatic fields [75] or strain field [76],[63] that would locally modify the bandgap [21]. For all these reasons, TMDs and metal monochalcogenides represent two promising families of materials for single photon emission purposes. In particular, the III-VI metal monochalcogenide [77] InSe (Indium Selenide) is the material under analysis in the first part of this work.

1.4 InSe as a promising 2D material for SPE

Although InSe has not been employed as single-photon emitter yet, it is one of the most promising materials listed so far to be exploited for this purpose. Similarly to the TMDs, it exhibits strong light-matter interaction and a reduced valley hybridization which in turn leads to a little dispersion of the defect state. Furthermore it owns a wide bandgap which can be tuned thank to the possibility of InSe to form many alloys (in Chapter 5 we will investigate InGaSe alloys with different In/Ga fractions). However, the most important characteristic of InSe is that it can be exfoliated into a stable 2D phase allowing for an easy manipulation of its lattice. It is important to highlight, however, that this material shows high sensitivity to air and device fabrication processes which can cause structural damages [78]. In order to protect its excellent electronic and optical properties, therefore, it is always required an effective passivation of the material based on the encapsulation of the monolayer. This is performed by covering the 2D InSe layer entirely between two sheets of a more stable material such as graphene [77] or hBN [78]. In the following section we will provide a more complete description of this material.

1.4.1 InSe Bulk and 2D Structure

InSe is a layered compound which is composed by the stacking of many monolayers, each of them in turn consists of four atomic layers of Se-In-In-Se that are bound together by strong covalent bonds with some ionic character [79],[80]. A monolayer is

itself bound to one another by Van der Waals interactions [79],[80]. Depending on the way they are stacked, three different polytypes are possible:

- β phase belongs to the hexagonal $P6_3/mmc$ space group [67] and it refers to the case in which there is a rotation of π around an axis perpendicular to the plane of the layer followed by a translation parallel to this axis [79];
- γ phase belongs, instead, to the trigonal $R\bar{3}m$ space group [67] and this time there is a horizontal translation of $+\frac{\mathbf{a}_1 + \mathbf{a}_2}{3}$ [79] where \mathbf{a}_1 and \mathbf{a}_2 are the basis vectors;
- ϵ phase is specular to the γ one (horizontal translation of $-\frac{\mathbf{a}_1 + \mathbf{a}_2}{3}$) [79].

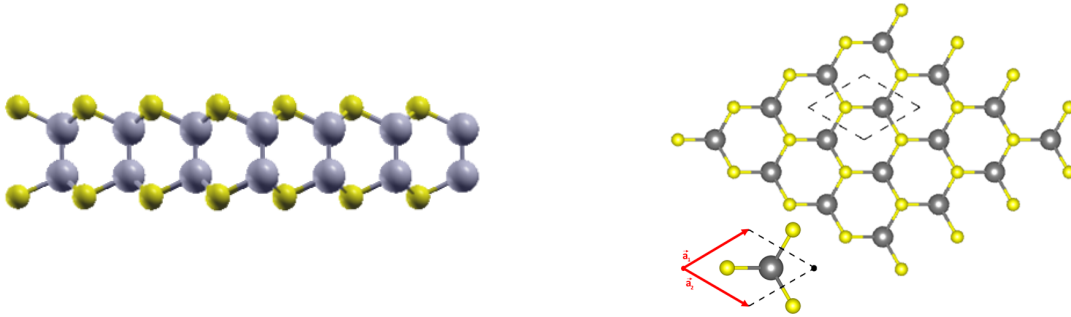


Figure 1.6: Side view (on the left) and top view (on the right) of a single layer of InSe (yellow and grey spheres represent Se and In atoms, respectively)

In order to better understand the different structures, figures 1.6 and 1.7 have been reported here. Figure 1.6 shows a single monolayer of InSe (notice that it is formed, as already said, by four layers of atoms, Se atoms in yellow and In atoms in grey) and the top view of the 1D material, while Figure 1.7 reports the primitive cells of the two most important InSe polytypes (i.e. β and γ phases) [82]. However, it is important to highlight that γ -InSe is inherently unstable and for this reason its practical application either in electronics or optoelectronics is hindered [71],[83], while β -InSe is the more energetically favorable phase and shows a good stability [71]. According to the reference article [67], the binding energy E_b between two layers is of the order of $\approx 60meV/atom$ for both cases which is very close to the one of the graphite [84] and of TMDs [85], meaning that the building blocks of InSe are only weakly coupled to each other. As a consequence, it is easy to separate the different monolayers. In order to insulate one them, several techniques are possible. The easiest solution is to exploit graphene-like exfoliation processes, however another effective synthesis method consists in the controlled growth of InSe onto a SiO_2 substrate. A silicon boat containing the InSe powder is placed in the center of a quartz tube. A piece of Si wafer covered with a thin layer of SiO_2 works as substrate for the sample growth. In order

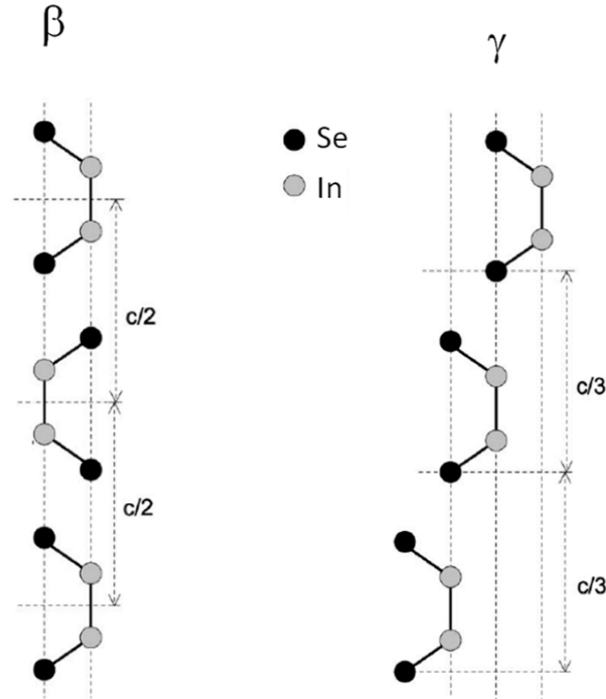


Figure 1.7: Image taken from reference [81] showing β polytype primitive cell (on the left) and γ polytype primitive cell on the right (hexagonal unit cell extending over three layers [79])

to provide an inert atmosphere and to carry the vaporized InSe gas to be deposited, an Ar flow is injected into the tube with a controlled flow rate. Depending on the working temperature and on the growth time the thickness of the material can be controlled with high precision [86]. The dynamical stability of the InSe monolayer has been proved observing its phonon dispersion curve along the high-symmetry directions, no imaginary frequencies are present [67] thus the material is stable.

1.4.2 InSe optical and electronic properties

For what concerns the electronic properties of the material, InSe shows in its bulk phase a direct bandgap of $\approx 1.1\text{eV}$ for β -InSe [67], but when reducing the number of stacked layers, it is possible to observe a direct-to-indirect transition. Depending on the method exploited to calculate the monolayer energy gap, the result can be very different, indeed the use of a simple DFT approach leads to an underestimation of this value, however, as mentioned in the article [67], the exploitation of more advanced methods simply leads to a rigid shift of the bandgap, thus all the considerations about the shapes of the CB and VB are valid in both cases (a more precise discussion on this point is presented in section 3.2.2). In general, anyway, independently on the

exploited method, the bandgap of the monolayer is greater than the one of the bulk phase. Decreasing dimensions, indeed, the quantum confinement effect becomes more relevant and bandgap increases (bandgap dependence on layer thickness). E_g obtained for a monolayer of InSe varies by varying the calculation method, in particular reference [87] reports an energy gap of 1.39 eV at GGA-PBE level, 2.21 eV for a hybrid HSE06 calculation and 2.93 eV with GW0 correction. In these calculations, the Spin Orbit Coupling (SOC) has not been considered; a more precise analysis on this topic is reported in the section 3.2.3. Taking the figure 1.8 as reference, it can be noticed

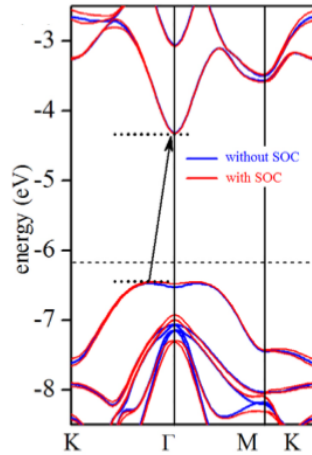


Figure 1.8: InSe monolayer band diagram example [87]

that the Conduction Band Minimum (CBM) is placed in Γ , while the Valence Band Maximum (VBM) along the $K \rightarrow \Gamma$ direction (near Γ). An almost flat VB dispersion around the Γ point indicates that electrons can easily be transferred between energetically near states with a small amount of thermal energy [70]. Furthermore, also the presence of two clearly visible maxima around this point (the so called sombrero-shaped dispersion) enhances the probability of electronic transitions between VB and CB. Indium selenide also shows low electron effective mass $m^* \approx 0.143m_0$, high electron mobility $\mu_e \approx 10^3 \text{ cm}^2 \text{ V}^{-1} \text{ s}^{-1}$ and good optical activity, making it suitable for many applications such as 2D graphene/InSe heterostructure-based photodetectors and 2D InSe-based FET with high current on/off ratio ($\approx 10^8$) [80].

CHAPTER 2

Methods

In the last decades, *ab initio* atomistic approach has emerged as a powerful tool able to predict material properties starting from a quantum description of the electrons. Among the possible methods proposed to solve the Schrödinger equation of a complex many-body system, the Density Functional Theory (DFT) is one of the most employed to derive the ground state properties of the mentioned system.

In this Chapter, the theoretical background of DFT and along with this also some technical details of its implementation such as the pseudopotential approach and the use of finite basis sets will be described.

2.1 The adiabatic approximation

The quantum mechanical description of interaction among electrons and nuclei is given by the Hamiltonian written in atomic units:

$$\begin{aligned} \mathcal{H} = & -\frac{1}{2} \sum_i \nabla_i^2 - \frac{1}{2M_I} \sum_I \nabla_I^2 + \frac{1}{2} \sum_{i \neq j} \frac{1}{|\mathbf{r}_i - \mathbf{r}_j|} + \\ & + \sum_{i,I} \frac{Z_I}{|\mathbf{r}_i - \mathbf{R}_I|} + \frac{1}{2} \sum_{I \neq J} \frac{Z_I Z_J}{|\mathbf{R}_I - \mathbf{R}_J|} \end{aligned} \quad (2.1)$$

where M_I is the ion mass divided by the electron mass (m_e), Z_I is the atomic number of the I -th ion, \mathbf{r}_i denotes the position of the i -th electron and \mathbf{R}_I is the position of I -th nucleus. The many-particle Hamiltonian in 2.1 cannot be solved without simplifications. The main approximation consists of the adiabatic or Born-Oppenheimer approximation. The ions are much heavier than the electrons, so they move much more slowly. The frequencies of ionic vibrations in solids are typically less than $10^{13} s^{-1}$, whereas the frequencies of electronic motion in semiconductors are of the order of $10^{15} s^{-1}$ because of the notable mass difference ($\frac{m_e}{M_n} \sim 10^{-3}$). As a result, electrons can respond to ionic motion almost instantaneously or, in other words, to the electrons the ions are stationary. On the other hand, ions cannot follow the motion of the electrons and they

see only a time-averaged electronic potential (V_i). If the Born-Oppenheimer approximation holds, the Hamiltonian in eq. 2.1 can be expressed as the sum of these terms:

$$\mathcal{H} = \mathcal{H}_{ions}(\{\mathbf{R}_I\}) + \mathcal{H}_e(\{\mathbf{r}_i\}, \{\mathbf{R}_{I0}\}) + \mathcal{H}_{e-ion}(\{\mathbf{r}_i\}, \{\delta\mathbf{R}_I\}) \quad (2.2)$$

where $\mathcal{H}_{ions}(\{\mathbf{R}_I\})$ is the Hamiltonian describing the ionic motion, $\mathcal{H}_e(\{\mathbf{r}_i\}, \{\mathbf{R}_{I0}\})$ is the Hamiltonian for the electrons with the ions frozen in their equilibrium positions \mathbf{R}_{I0} and $\mathcal{H}_{e-ion}(\{\mathbf{r}_i\}, \{\delta\mathbf{R}_I\})$ represents the change in the electronic energy as result of the displacements $\delta\mathbf{R}_I$ of the ions from their equilibrium positions. $\mathcal{H}_{e-ion}(\{\mathbf{r}_i\}, \{\delta\mathbf{R}_I\})$ is known as the electron-phonon interaction term.

The electronic Hamiltonian $\mathcal{H}_e(\{\mathbf{r}_i\}, \{\mathbf{R}_{I0}\})$ and the ionic Hamiltonian $\mathcal{H}_{ion}(\{\mathbf{R}_j\})$ are given by:

$$\mathcal{H}_e(\{\mathbf{r}_i\}, \{\mathbf{R}_{I0}\}) = -\frac{1}{2} \sum_i \nabla_i^2 + \frac{1}{2} \sum_{i \neq j} \frac{1}{|\mathbf{r}_j - \mathbf{r}_i|} + \sum_{i,I} \frac{Z_I}{|\mathbf{r}_i - \mathbf{R}_{I0}|} \quad (2.3)$$

$$\mathcal{H}_{ions}(\{\mathbf{R}_I\}) = \sum_I \frac{\mathbf{P}_I^2}{2M_I} + V_i(\{\mathbf{R}_I\}) \quad (2.4)$$

This approximation allows to treat separately the electronic and ionic contributions considering "quantum mechanical" electronic character and the more "classical" ionic behavior. However describing the electronic structure problem, Eq. 2.3, remains a quantum many-body problem that is very difficult to solve since for a N_e electrons the many-body wave function is then function of $3N_e$ space variables, $\psi(\mathbf{r}_1 \dots \mathbf{r}_{N_e})$, where \mathbf{r}_i ($i = 1 \dots N_e$) is a 3 dimensional position vector neglecting the spin variables. An accurate method to overcome the drawback is described in the following section (2.2).

2.2 Density functional theory

Density Functional Theory (DFT) is a mean-field approach to describe a system of many interacting electrons that was formulated in the sixties by Hohenberg and Kohn [88] and Kohn and Sham [89]. DFT is a theory for the electronic structure formulated in terms of the electron density as basic unknown, instead of the electronic wavefunction. Since the density of particles in the ground state plays a central role in the theory, it can be considered as a "basic variable" and all properties of the system can be considered to be unique functionals of the ground state density. DFT can be regarded as the direct descendant of the Thomas-Fermi theory (1927) [90, 91]. Although Thomas-Fermi approximation is not accurate the approach illustrates the way DFT works. In the Thomas-Fermi method the kinetic energy of the system of electrons is approximated as an explicit functional of the density, idealized as non-interacting electrons in a homogeneous gas with density equal to the local density at any given point. Dirac improved this model and formulated the local approximation for exchange that is still

in use today [92]. In this section the basic formalism of the theory is presented starting from the fundamental Hohenberg and Kohn theorems which demonstrate the central role played by the electron density in quantum mechanics.

2.2.1 The Hohenberg-Kohn theorems

Consider a system of N electrons enclosed in a box and moving under the influence of some time-independent local external potential $V(\mathbf{r})$.

The first Hohenberg-Kohn theorem demonstrates that, for a system with a fixed number of particles, $V(\mathbf{r})$ is determined within an additive constant, once the electron density $n(\mathbf{r})$ is known. This means that the density determines univocally the external potential, and consequently the Hamiltonian and all electronic properties of the system. The ground state properties of a many-electron system are uniquely determined by a function (the electron density) that depends on only 3 spatial coordinates, reducing the many-body problem of N electrons with $3N$ spatial coordinates to 3 spatial coordinates, through the use of functionals of the electron density. According to this statement, the ground state expectation value of any observable is a unique functional of the ground state density n_0 . In this formalism the total energy can be written as:

$$E_v[n] = \int n(\mathbf{r}) v(\mathbf{r}) d\mathbf{r} + F[n] \quad (2.5)$$

The functional $F[n]$ is a universal functional, which includes the kinetic and electron-electron repulsion energy and it is unique in the sense that it does not depend on the external potential which acts on the system.

The second Hohenberg-Kohn theorem defines an energy functional for the system and proves that the correct ground state electron density is the one that minimizes this energy functional.

$$E_0 \leq E[\tilde{n}] \quad (2.6)$$

The proof is based on the variational principle as for any trial wave function $\tilde{\psi}$:

$$\langle \tilde{\psi} | H | \tilde{\psi} \rangle = \int \tilde{n}(\mathbf{r}) v(\mathbf{r}) d\mathbf{r} + F[\tilde{n}] = E_v[\tilde{n}] \geq E_v[n] \quad (2.7)$$

Equality stands only in the true ground-state. The variation of the total energy with respect to a change of $n(\mathbf{r})$ at constant number of electrons (N)

$$\delta \left\{ E_v[n] - \mu \left[\int n(\mathbf{r}) d\mathbf{r} - N \right] \right\} = 0 \quad (2.8)$$

leads to the Euler equation:

$$\mu = \frac{\delta E_v[n]}{\delta n} = v(\mathbf{r}) + \frac{\delta F_{HK}[n]}{\delta n} \quad (2.9)$$

where the Lagrange multiplier μ is the chemical potential.

2.2.2 The Kohn-Sham equations

The ground state electron density can be in principle determined by solving the Euler equation 2.9; however, the exact form of the functional ($F[n]$) is unknown. Kohn and Sham [89] proposed a scheme to solve the multielectronic problem in which, starting from a model of non interacting electron system, they obtain a single particle Schrödinger equation whose solution gives the same electron density of the interacting electron system. It is first convenient to define a new functional $G[n(\mathbf{r})]$, obtained from $F[n(\mathbf{r})]$ by subtracting the term of the electron-electron electrostatic repulsion:

$$G[n(\mathbf{r})] = F[n(\mathbf{r})] - \frac{1}{2} \int d\mathbf{r} \int d\mathbf{r}' \frac{n(\mathbf{r}) n(\mathbf{r}')}{|\mathbf{r} - \mathbf{r}'|} \quad (2.10)$$

It is then useful to extract the kinetic energy functional T_s of the non-interacting system from $G[n(\mathbf{r})]$, isolating all the exchange and correlation contributions:

$$G[n(\mathbf{r})] = T_s[n(\mathbf{r})] + E_{xc}[n(\mathbf{r})] \quad (2.11)$$

In this way the total energy functional expressed in eq. 2.5 becomes:

$$E[n(\mathbf{r})] = \int n(\mathbf{r}) v(\mathbf{r}) d\mathbf{r} + T_s[n(\mathbf{r})] + \frac{1}{2} \int d\mathbf{r} \int d\mathbf{r}' \frac{n(\mathbf{r}) n(\mathbf{r}')}{|\mathbf{r} - \mathbf{r}'|} + E_{xc}[n(\mathbf{r})] \quad (2.12)$$

The variation of the previous expression as a function of the number of electrons N leads to the following Euler equation:

$$\mu = \frac{\delta T_s[n]}{\delta n} + \int d\mathbf{r}' \frac{n(\mathbf{r}')}{|\mathbf{r} - \mathbf{r}'|} + v(\mathbf{r}') + \frac{\delta E_{xc}[n]}{\delta n} \quad (2.13)$$

$$\mu = V_{KS}(\mathbf{r}') + \frac{\delta T_s[n]}{\delta n} \quad (2.14)$$

where $V_{KS}(\mathbf{r})$ is the Kohn-Sham potential consisting of the external potential, the classical Coulomb potential (Hartree potential) and the exchange-correlation potential. If one now considers the variation of the total energy expressed with respect to the one electron wave function ψ_i , with the constraint of orthonormality of the ψ_i

$$\int \psi_i^*(\mathbf{r}) \psi_j(\mathbf{r}) d\mathbf{r} = \delta_{ij} \quad (2.15)$$

one obtains:

$$h_{KS}\psi_i = \left[-\frac{1}{2} \nabla^2 + V_{KS}(\mathbf{r}) \right] \psi_i = \sum_{j=1}^N \epsilon_{ij} \psi_j \quad (2.16)$$

Making use of the fact that the operator h_{KS} is Hermitian, a unitary transformation of the orbitals leads to the Kohn-Sham equation:

$$\left[-\frac{1}{2} \nabla^2 + V_{KS}(\mathbf{r}) \right] \phi_i = \epsilon_i \phi_i \quad (2.17)$$

Once solved this equation, it is possible to obtain the electron density of the interacting system as:

$$n(\mathbf{r}) = \sum_i^N |\phi_i(\mathbf{r})|^2 \quad (2.18)$$

This may be the most important equation of the DFT. It states that the motion of the interacting electrons can be treated exactly as a system of non-interacting particles. The electrons can be considered as if they move in a common effective potential V_{KS} . All the interaction between the electrons can be merged exactly into a single potential V_{KS} . Once $n(\mathbf{r})$ is obtained, all the other observable can be derived.

Although DFT is an exact theory of the ground state, it is affected by the limit that the expression of the exchange and correlation potential is not known explicitly. Different formulations of this functional have been proposed in the literature, based on different theoretical arguments. The simplest one is the so called Local Density Approximation followed by the generalized gradient approximation (GGA), meta-GGA, hybrid forms rely on a Jacob's Ladder of progressively more complicated approximations to the many-body exchange-correlation (XC) density functional [93].

2.2.3 LDA and GGA approximation

In the previous sections the many body problem was reduced into the form of a single particle problem, by means of an exact formalism. The whole complexity of the electron-electron interaction was confined in the exchange-correlation term. Since DFT does not provide the analytical expressions of the functional $E_{xc}[n]$, the practical application of the theory requires the choice of approximated forms for $E_{xc}[n]$. Over the years many approximate expression have appeared, the most simple and widely used of which is the local density approximation (LDA) [94, 95]. In a homogeneous gas of interacting electrons the density is constant and the exchange-correlation energy per particle $\epsilon_{xc}(n)$ is a function (not a functional) of the density. The total exchange-correlation energy is obtained by multiplying $\epsilon_{xc}(n)$ by the total number of electrons present in the gas:

$$E_{xc}[n] = N\epsilon_{xc}(n) \quad (2.19)$$

Within the local density approximation, the non-homogeneous electron gas is treated in complete analogy: the total exchange-correlation energy is obtained by accumulating the contributions from every portion of the non-uniform gas as if it was locally uniform:

$$E_{xc}^{LDA} = \int n(\mathbf{r})\epsilon_{xc}^{hom}(n(\mathbf{r})) d\mathbf{r} \quad (2.20)$$

In calculating the integral 2.20 the function $\epsilon_{xc}^{hom}(n)$ is evaluated for the local density $n(\mathbf{r})$ of the inhomogeneous system under consideration: $\epsilon_{xc}^{hom}(n) = \epsilon_x^{hom}(n) + \epsilon_c^{hom}(n)$ is the exchange and correlation energy per electron in the homogeneous electron gas of density n . LDA is exact for an uniform system and is expected to be valid for systems

with slowly varying electron density. For all the other cases the LDA approximation is indeed uncontrolled; its justification relies mainly upon its ability to reproduce the experimental ground-state properties of a large number of solids. LDA performs best for metals, while for semiconductors and insulators the band gap is underestimated by up to 50 % in some cases, but this problem is not only pertinent to LDA, but also to the formally not-justified interpretation of the Kohn-Sham eigenvalues as excitation energies.

A number of methods have been developed to correct the deficiencies of the LDA. For a system of nonuniform density, E_{xc} is no longer adequately reproduced by Eq. 2.20. A simple modification appears to be the inclusion of gradient terms ∇n , which leads to the Generalized Gradient Approximation (GGA) [96],

$$E_{xc}^{GGA} = \int f(n, \nabla n) d\mathbf{r} \quad (2.21)$$

Various recipes for constructing $f(n, \nabla n)$ have been proposed. The PBE (Penede, Burke and Ernzerhof) form [97] is probably the simplest GGA functional. The form for the correlation in this case is expressed as the local correlation plus an additive term both of which depend upon the density gradient.

It is found that even if LDA/GGA functionals describe poorly the electronic properties of the systems, as the well known problem of the underestimation of the energy gap, the total energy of the system that they give is quite good, i.e. the structural properties are adequately reproduced.

2.3 The Hellmann-Feynman theorem

Suppose to know the ground state eigenfunction ψ_R for a system in a fixed configuration of nuclei $\{\mathbf{R}_I\}$, solving the equation $\mathcal{H}\psi_R = E\psi_R$, the energy will be given by:

$$E = \frac{\langle \psi_R | \mathcal{H}(\mathbf{R}) | \psi_R \rangle}{\langle \psi_R | \psi_R \rangle} \quad (2.22)$$

Thus, the force on a nucleus n will be given by the negative gradient of the energy with respect to its coordinates (\mathbf{R}_n):

$$\mathbf{F}_n = -\nabla_n E = -\nabla_n \left[\frac{\langle \psi_R | \mathcal{H}(\mathbf{R}) | \psi_R \rangle}{\langle \psi_R | \psi_R \rangle} \right] \quad (2.23)$$

When deriving the term at the right side of equation 2.23, one must observe that not only the Hamiltonian but also the ground state depend on the particular configuration \mathbf{R} . The Hellmann-Feynman theorem [98, 99] states that this dependence can be neglected if ψ_R is an eigenstate of the Hamiltonian. Thus, equation 2.24 gives:

$$\nabla_n E = \frac{\langle \psi_R | \nabla_n \mathcal{H}(\mathbf{R}) | \psi_R \rangle}{\langle \psi_R | \psi_R \rangle} \quad (2.24)$$

This means that in order to obtain the forces acting on atoms in a particular geometric configuration, it is enough to know the explicit dependence of the Hamiltonian on the nuclear coordinate of the system. Once the forces acting on atoms are known one can integrate the classical equation of the motion and study the evolution of the system or find the minimum energy structure.

2.4 Practical aspects of DFT implementation

In the following paragraphs some practical aspects regarding DFT implementation in computer codes will be discussed, namely, the use of pseudopotential and the use of basis sets to expand the system wave-function.

2.4.1 Basis set

In DFT method the aim to compute properties of interest without recourse to experimental data requires solving the Kohn-Sham equations and finding the ground state wavefunction. Eigenfunctions are usually expanded in terms of a set of a complete basis set. A single electron wavefunction can be written as:

$$\psi_i(\mathbf{r}) = \sum_{j=1}^{\infty} c_j \phi_j(\mathbf{r}) \quad (2.25)$$

where $\phi_j(\mathbf{r})$ are members of a complete set of functions. Obviously it is impossible to use an infinite number of basis functions so the sum in 2.25 is taken over a finite number of functions. This introduces a source of error into the calculations, which has to be minimized. Any family of functions could, in principle, be used as basis functions. Ideally the basis functions should have the same limiting behaviour as the real wavefunction, for an isolated atom or molecules they should decay to zero, and they should be computationally inexpensive.

Plane Wave basis set

Ions in a perfect crystal are arranged in a regular periodic way (at $0K$), therefore the external potential felt by the electrons is periodic and the period is the same as the length of the unit cell (l). The external potential on an electron at \mathbf{r}_i can be expressed as $V(\mathbf{r}) = V(\mathbf{r} + l)$. For these kind of systems, the Bloch Theorem hold, and the wavefunction can be written as the product of a cell periodic part and a wave-like part:

$$\phi_{i,\mathbf{k}} = u_{i,\mathbf{k}}(\mathbf{r})e^{i\mathbf{k}\cdot\mathbf{r}} \quad (2.26)$$

where $u_{i,\mathbf{k}}(\mathbf{r})$ is a function that has the lattice periodicity. The periodic part of the wave function can be expanded using a basis set of plane waves whose wave vectors \mathbf{G}

are the reciprocal lattice vectors of the crystal:

$$u_{i,\mathbf{k}}(\mathbf{r}) = \sum_{\mathbf{G}} c_{i,\mathbf{G}} e^{i\mathbf{G}\cdot\mathbf{r}} \quad (2.27)$$

therefore each electronic wave function can be written as a linear combination of plane waves (PW):

$$\phi_{i,\mathbf{k}} = \sum_{\mathbf{G}} c_{i,\mathbf{k}+\mathbf{G}} e^{i(\mathbf{k}+\mathbf{G})\cdot\mathbf{r}} \quad (2.28)$$

the $c_{i,\mathbf{k}+\mathbf{G}}$ are unknown and must be determined for each specific case. The plane-waves basis set is in principle infinite, but in real calculations it is reduced to a finite one by truncating the sum over \mathbf{G} to include only those plane waves with a kinetic energy $E_k = \frac{1}{2}(\mathbf{k} + \mathbf{G})^2$ less than a given energy cutoff (E_{cut}). This truncation will lead to an error in the computed total energy. At variance with other techniques (and basis sets) the convergence of the plane-wave basis set (and thus the error) can be controlled simply by increasing the cutoff energy. When pseudopotentials are used (see next paragraph) to include the electron/ion interaction, it is possible to reduce sensibly the cutoff energies, without losing accuracy.

2.4.2 Pseudopotential theory

A pseudopotential (or effective potential) is used as an approximation for the simplified description of ion potentials. The pseudopotential is an attempt to replace the complicated effects of the core electrons of an atom and its nucleus with an effective potential so that the Schrödinger equation contains a modified effective potential term. When considering a solid, the strong changes in crystal potential (Coulomb singularity) induce strong oscillations in valence electronic wavefunctions near the atomic nuclei. This is due to the fact that valence electronic wavefunctions must be always orthonormal to atomic core wavefunctions. Whereupon for a correct approximation of this oscillations a high number of PW need. This problem has been overcome by Phillips and Kleinman introducing the Pseudopotential method [100].

To introduce this concept we have to focus on an isolated atom with spherical symmetry. The Schrödinger equation for some spherical potential $V(r)$ is:

$$\left[-\frac{1}{2} \frac{d^2}{dr^2} + \frac{l(l+1)}{2r^2} + V(r) - \epsilon \right] \phi_l(r) = 0. \quad (2.29)$$

Here $\phi_l(r)$ is the radial part of the wave function related to the full wavefunction $\psi(\mathbf{r})$ via $\psi(\mathbf{r}) = (1/r)\phi_l(r)Y_{lm}(\theta, \phi)$ is a spherical harmonic.

The ionic potential acting on the electrons $V_{ext} = \sum_I \frac{Z_I e^2}{|\mathbf{r}-\mathbf{R}_I|}$ consists of a series of Coulomb potentials which diverge at the ion position as $\sim r^{-1}$ where $r \rightarrow 0$. The theory of pseudopotentials allows one to replace the potential V_{ext} with a much softer potential \hat{V}_{PS} that can be treated more easily in the numerical calculations.

In what follows, there will be a description of a scheme to replace the Coulomb potential Ze/r of the ion having charge Z with a softer potential having similar scattering properties in the relevant energy window. This particular pseudopotential can be written in the form

$$\hat{V}_{PS} = V_{loc}(r) + \sum_i D_{ii'} |\beta_i\rangle \langle \beta_{i'}| \quad (2.30)$$

with an appropriately chosen potential V_{loc} and orbitals β_i that vanish outside the core region.

Ultrasoft pseudopotentials

The Ultrasoft pseudopotentials, which were developed by Vanderbilt [101], attain much smoother (softer) pseudo-wavefunctions with respect to other possible schemes, such as for example norm-conserving pseudopotentials, so use considerably fewer plane-waves for calculations of the same accuracy. Typically, the cutoff energy E_{cut} when using ultrasofts is about half that of conventional norm-conserving pseudopotentials.

This approach includes an overlap operator \hat{S} that appears on the right side of the secular equation:

$$\left[-\frac{1}{2} \frac{d^2}{dr^2} + \frac{l(l+1)}{2r^2} + \hat{V}^{PS} \right] \phi_{l\tau}^{PS}(r) = \epsilon_{l\tau} \hat{S} \phi_{l\tau}^{PS}(r) \quad (2.31)$$

turning this equation into a generalized eigenvalue problem. The index τ here distinguishes between multiple solutions for the same value of l . Furthermore, we require the generalized eigenfunctions $\phi_{l\tau}^{PS}$ to satisfy the generalized orthonormalization condition $\langle \phi_{l\tau}^{PS} | \hat{S} | \phi_{l'\tau'}^{PS} \rangle = \delta_{ll'} \delta_{\tau\tau'}$. Denoting indices l, m, τ by the single index i , we will again express the pseudopotential operator as [101] :

$$\hat{V}_{PS} = V_{loc}(r) + \sum_i D_{ii'} |\beta_i\rangle \langle \beta_{i'}| \quad (2.32)$$

Now we will define the operator \hat{S} in such a way that the energy derivative of the logarithmic derivative of the pseudo wavefunction will be reproduced for an arbitrary choice of the pseudo wavefunctions ϕ_i^{PS} . For this reason, in the ultrasoft scheme there is more freedom in choosing the pseudofunctions ϕ_i^{PS} and therefore they can be chosen to be more smooth than in other schemes.

We can define the pseudopotential \hat{V}_{PS} by

$$D_{ij} = B_{ij} + \epsilon_j Q_{ij} \quad (2.33)$$

and the operator \hat{S} as:

$$\hat{S} = 1 + \sum_{ij} Q_{ij} |\beta_i\rangle \langle \beta_j|. \quad (2.34)$$

With this choice of operators \hat{S} and \hat{V}_{PS} , the only imposed requirement on the pseudo-functions ϕ_i^{PS} is that they match the true all-electron wavefunctions beyond the cutoff radius. Additional terms arising from the introduction of operator \hat{S} makes ultrasoft pseudopotential method more complicated with respect to others. Nevertheless, this reduces the total computational cost.

2.4.3 Reciprocal-space integration and \mathbf{k} points sampling

When considering periodic systems, in the Kohn-Sham calculation scheme the valence electron density and the band structure energy are defined as sum over the entire BZ as follows:

$$n(\mathbf{r}) = \sum_v^{N_v} \sum_{\mathbf{k} \in BZ} |\phi_{v,\mathbf{k}}(\mathbf{r})|^2 \quad (2.35)$$

$$E_{band} = \sum_v^{N_v} \sum_{\mathbf{k} \in BZ} \epsilon_{v,\mathbf{k}} \quad (2.36)$$

when $N \rightarrow \infty$ the discrete sums are replaced by integrals over the Brilluoin Zone (BZ) and an average over the BZ of the \mathbf{k} -dependent functions is actually performed. In practice, it is possible to approximate the integral over the BZ by using a selected set of \mathbf{k} -points, exploiting both the space group of the crystal, and a clever sampling of the BZ. Due to the group symmetry the sum over \mathbf{k} can be restricted to the irreducible part of the BZ (IBZ), and then sample this zone with a special point technique. Typically, one employs a Monkhorst-Pack grid [102], which consists of a mesh of equally spaced points along the three reciprocal space primitive vectors and it is defined by three integer $(n_x \ n_y \ n_z)$. These n_i represent the number of sampling point along each lattice vectors, and of course, the larger are n_i the finer the grid will be and the more accurate will be the calculated electronic density. The actual n_i values to be used generally depends on the problem that needs to be solved; usually convergence test, at increasing n_i , have to be performed to determine for each specific system the grid that gives accurate results. For example, systems with a gap in the energy spectrum typically require fewer points, whereas in case of metallic systems a much denser \mathbf{k} -mesh must be employed, ensuring good sampling of the Fermi surface.

2.5 Cluster Expansion

The Cluster Expansion is a method used to predict alloy stability and concentration dependent phase diagrams. In this thesis work, in particular, CE has been used to study the $In_{1-x}Ga_xSe$ alloy and to calculate its most stable structures for different In/Ga fractions (see 5). In order to understand the *Cluster Expansion* method, it may be useful to start this section with a rapid review of the *Nearest-neighbor Ising model*. This one, indeed, is used to study spin systems, i.e. systems in which any component of the structure (for example electrons in a 1D chain or in a 2D lattice, in figure 2.1 two examples have been reported) can be in two different states (spin-up or spin-down). Depending on the number of spin-up (or down) and depending on their specific

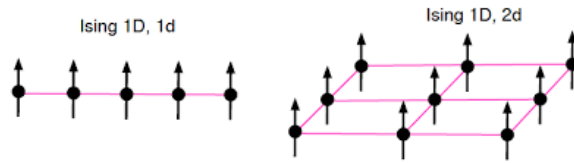


Figure 2.1: Ising model

positions in the lattice, the resulting total energy of the system will be different. In particular, its Hamiltonian can be expressed as follows [103]:

$$H(s) = C - \mu \sum_j^N h_j s_j + \sum_{\langle ij \rangle} J_{ij} s_i s_j$$

C is simply a scaling factor, μ is the electron's magnetic moment and h_j is the interaction of site j with an external magnetic field, N is the number of occupied lattice sites, J_{ij} is the interaction coefficient between lattice sites i and j , and $\langle ij \rangle$, finally, means that i and j are nearest neighbours. The same formalism, nevertheless, can be used to describe the configuration of binary alloys, i.e. whenever one is dealing with only two atomic species A and B. Instead of using ± 1 to represent "spin-up" and "spin-down" at each lattice site, in fact, one can let -1 represent the presence of element A and +1 represent the presence of element B [103], [104]. Under this assumption, the Hamiltonian can be rewritten as [104]:

$$H(\sigma_1, \dots, \sigma_M) = H^{\text{Ising}}(\sigma_1, \dots, \sigma_M) = J_0 + J_1 \sum_I \sigma_I + J_{2,1} \sum_{I=1}^M \sum_I^{D_{2,1}} \sigma_{I_1} \sigma_{I_2} \quad (2.37)$$

where:

- σ_I is the spin configuration of the I -th element ($\sigma_I = \pm 1$), i.e. if in the site I there is A or B;

- J_0 is an offset term which indicates the average energy of the entire lattice;
- J_1 is the self-interaction energy and it only counts the overall number of spins-up and down;
- $J_{2,1}$ is the more interesting term and it represents the nearest-neighbors interaction energy. Notice that the subscript 2 stands for "the interaction is only between two atoms", while the subscript 1 indicates that this coupling involves only the nearest neighbors;
- $D_{2,1}$ denotes the limits of the sum over the degenerate states of σ_I .

According to the previous formula, it is clear that the Ising model takes into account only two types of interactions (also called "clusters" or "figures"): the single component cluster (the second term in equation 2.37) and the nearest neighbor pair cluster (the third term of 2.37). The problem of this model, however, lies in the fact that interactions of ions in a binary alloy go beyond the nearest neighbours distance. For this reason, in order to obtain more precise results it is mandatory to expand \mathcal{H} to include interactions of additional atomic groups (Figure 2.2 taken from article [103]).

The Cluster Expansion arises from this assumption and it can be considered as a

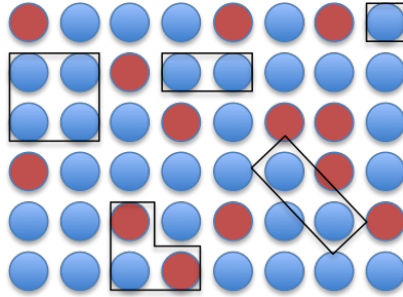


Figure 2.2: Different cluster examples

generalized Ising model in which also multiple pair interactions, triplet and quadruplet interactions and so forth (2.2) are included. The general Hamiltonian of the CE is therefore:

$$H(\sigma) = H^{CE}(\sigma) = \sum_f m_f J_f \langle \prod_{I \in f'} \sigma_I \rangle \quad (2.38)$$

which implicitly says that all possible types of clusters f that can be found among the lattice sites theoretically should be considered in the expansion (up to the N-body interaction which includes the entire lattice, [104]):

- f is a certain cluster;

- m_f is its multiplicity which takes into account degenerate clusters;
- J_f is the related energetic contribution, the Effective Cluster Interaction (ECI), and it is the analogous to the J coefficients of the Ising model;
- $\langle \prod_{I \in f'} \sigma_I \rangle$ is the normalized spin product (like $\sigma_i \sigma_j$ in the Ising model equation) of a particular cluster over the lattice and its average is taken over all the clusters f' equivalent to f by symmetry; as already said, the value of σ_I (± 1) depends on the atom placed in I-th site.

In principle, the CE theory is exact if one can manage to calculate the infinite expansion knowing all the ECIs, however, since it is impossible to deal with an almost infinite amount of variables, from a practical point of view, it is necessary to neglect some figures of the summation. Typically 10 to 20 ECIs are enough to accurately describe an alloy. The crucial part of the CE is therefore the determination of the interaction coefficients which can be derived either theoretically or experimentally. In this thesis work, ECIs coefficients have been extracted by computing the DFT energy of some of the possible alloy configurations [105]. As an example, let's consider that four different alloy arrangements have been calculated by DFT. At the end of simulations, one obtain a system of four equations (2.39), one for each configuration, that all share the same ECIs. According to the Cluster Expansion equation 2.38, one gets:

$$\begin{pmatrix} E_0 \\ E_1 \\ E_2 \\ E_3 \end{pmatrix} = \begin{pmatrix} \prod_1^0 & \prod_2^0 & \prod_3^0 & \prod_4^0 \\ \prod_1^1 & \prod_2^1 & \prod_3^1 & \prod_4^1 \\ \prod_1^2 & \prod_2^2 & \prod_3^2 & \prod_4^2 \\ \prod_1^3 & \prod_2^3 & \prod_3^3 & \prod_4^3 \end{pmatrix} \begin{pmatrix} J_0 \\ J_1 \\ J_2 \\ J_3 \end{pmatrix} \quad (2.39)$$

Energies calculated through DFT provide the vector on the left-hand side of 2.39, while the central matrix is known since the alloy structure is the input of the DFT calculation, thus J values can be found by simply inverting the matrix:

$$\begin{pmatrix} J_0 \\ J_1 \\ J_2 \\ J_3 \end{pmatrix} = \begin{pmatrix} \prod_1^0 & \prod_2^0 & \prod_3^0 & \prod_4^0 \\ \prod_1^1 & \prod_2^1 & \prod_3^1 & \prod_4^1 \\ \prod_1^2 & \prod_2^2 & \prod_3^2 & \prod_4^2 \\ \prod_1^3 & \prod_2^3 & \prod_3^3 & \prod_4^3 \end{pmatrix}^{-1} \begin{pmatrix} E_0 \\ E_1 \\ E_2 \\ E_3 \end{pmatrix} \quad (2.40)$$

Once ECIs have been determined, one can use equation 2.38 to calculate the energies of any other configuration without the need to use DFT calculations (i.e. this time the unknown is $E(\sigma)$). The higher is the number of terms that are considered in the expansion, the smaller is the error that one commits. If the ECIs accuracy is not satisfactory, other DFT calculations are performed on other configurations. The construction of a phase diagram for the alloy is therefore a step by step process that involves alternatively one DFT and one CE calculation; in particular, at each step, we choose the most appropriate input structure for the next DFT calculation which in turn

provides a new energy to be used for the expansion. Since the system 2.39 is solvable only if the number of ECIs coincides with the number of DFT calculated energies, for each new energy returned, the summation (2.38) is expanded of one coefficient and an equation is added to 2.39. After that, as previously discussed, one is able to find the new expansion coefficient J_n by exploiting 2.40. The power of this method is that, once one has determined a sufficiently high number of ECIs, it allows for the prediction of the energy of all configurations for the full concentration range, accessing also those arrangements that are too computational demanding for an *ab-initio* approach. The method is stopped when an accuracy threshold for the ECIs is reached. The carefulness of results is provided by the so-called cross-validation score parameter: when it becomes smaller than $k_B T$ ($\approx 25\text{meV}$ at room T) it means that coefficients of the expansion are reliable and the process can be interrupted.

CHAPTER 3

Computational approach and accuracy tests

In this thesis work, all the simulations have been performed in the frame of Density Functional Theory. More in detail, we have used the Perdew, Burke and Ernzerhof (PBE) GGA functional since, despite the already mentioned problem related to the underestimation of the energy gap, it adequately reproduces the structural properties as well as the electronic one of large classes of materials. The use of Ultrasoft pseudopotentials attains much smoother pseudo-wavefunctions thus it requires fewer Plane Waves for calculations of the same accuracy. Furthermore, as for most DFT codes that use Plane Wave basis set expansion, the program is built to deal with periodic systems, therefore periodic boundary conditions are applied to the simulation cell. Before starting a simulation, considering some numerical aspects of DFT implementation, and in particular taking into account the two sections 2.4.1 and 2.4.3, some computational conditions must be defined to achieve desired accuracy. In particular, we have to properly specify the PW basis set cutoff energy (3.1.1), the number of sampling k-points in the Brillouin Zone (BZ) (3.1.2), the dimensions of the simulation cell (3.2.1) and the pseudopotential for each atomic species (3.2.3). In order to avoid numerical errors that could lead to inaccurate results, some tests are required to prove that the chosen computational conditions are suitable to get reliable calculations. In our specific case, the cutoff energy and the number of k-points have been estimated for the bulk phase of InSe, while tests concerning the determination of the equilibrium lattice parameters and the role of spin-orbit coupling have been performed directly on the InSe monolayer. As reference model system for our tests, we chose β -InSe bulk structure, indeed, as already mentioned in the paragraph 1.4, γ -InSe is an inherently unstable phase thus its practical exploitation in electronics and optoelectronics is hindered (see figures 1.6 and 1.7 as reference).

3.1 β -InSe

3.1.1 PW cutoff energy convergence

We first estimated a proper value of the wave function cutoff energy, indeed the trade-off between a satisfactory precision of the results, which increases along with the cutoff, and an acceptable computational cost, which scales with N_{PW}^2 (where N_{PW} is the total number of plane waves in the basis set) is always an issue (2.4.1).

According to the values found in the reference [82], we initially set $\mathbf{a}=\mathbf{b}$ (the lattice

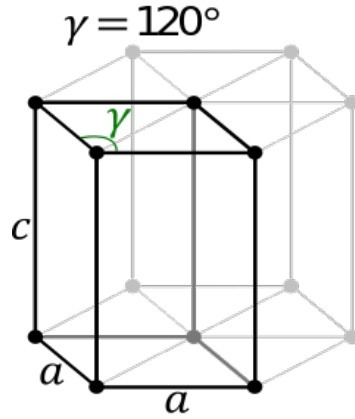


Figure 3.1: Hexagonal unit cell

parameter) to 7.718 au (i.e. 4.084 Å) and $\mathbf{c}= 33.165$ au (17.550 Å). At these lattice parameters the cutoff energy has been varied from 20 to 60 Ry and for each of these values we analysed the variation of the total energy of the system per the primitive cell. Results are reported in figure 3.2.

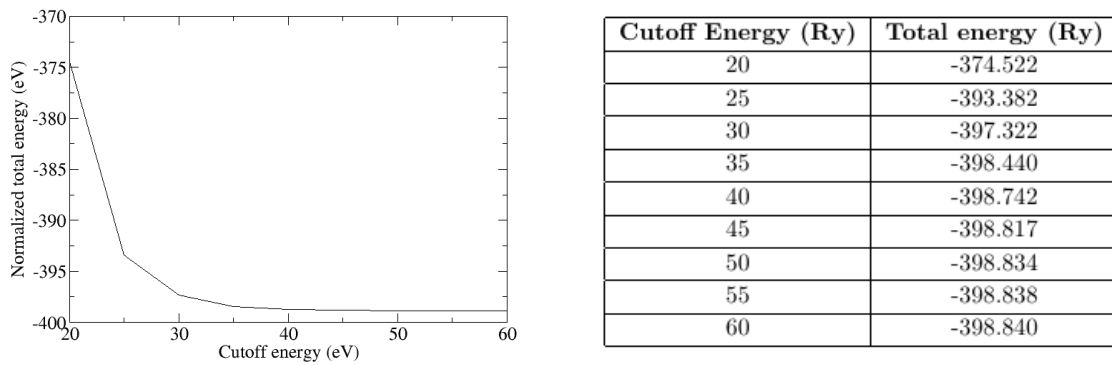


Figure 3.2: β -InSe primitive cell energies for different cutoffs with lattice parameter set to $\mathbf{a}=7.718$ au

Convergence is achieved for a cutoff energy of 45 Ry, where the energy variation between

two consecutive cutoffs becomes $< 0.02Ry$ (see figure 3.3). It is interesting to notice that, according to the variational theorem, the higher is the accuracy of the calculation (which increases along with the cutoff), the smaller (more negative) is the total energy of the system thus ΔE is always a positive quantity (3.3).

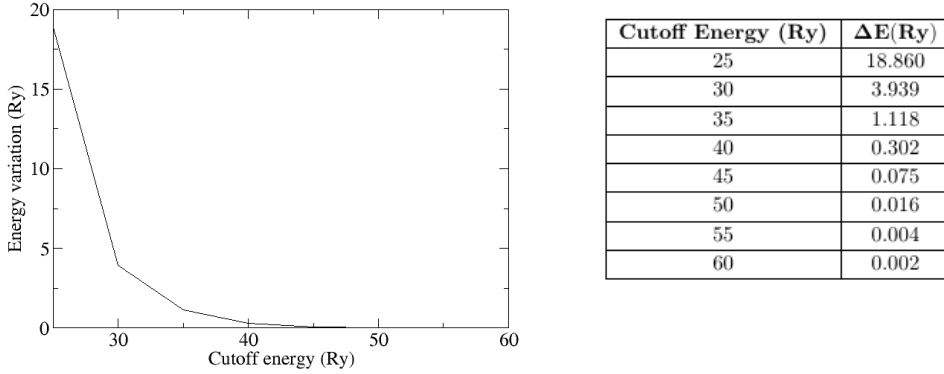


Figure 3.3: Variation of the total energy difference (ΔE) of the β -InSe primitive cell for two consecutive cutoff values

3.1.2 K-points sampling convergence

Accuracy tests were performed to obtain the number of k-points to be considered to sample the Brillouin zone (BZ) (2.4.3) of bulk InSe and to obtain converged energies. Under the same conditions of the previous test (but at constant cutoff energy of 45 Ry), the number of sampled k-points has been varied along the three BZ directions by considering several Monkhorst-Pack (MP) grids, from (1 1 1) to (8 8 8). These three indexes indicate the number of sampled points in the reciprocal space along the x , y and z directions, respectively. In order to select the more suitable MP grid, we have considered the energy of the primitive cell as a function of the grid size. Results are reported in figure 3.4.

Results show that a (2 2 2) grid gives already converged total energy (indeed ΔE with respect to the (3 3 3) case is $\approx 0.007 Ry$).

3.2 2D InSe monolayer

3.2.1 Equilibrium structure

Having found the best PW cutoff and k-point sampling grid for β -InSe, we then predicted the equilibrium structure for an InSe monolayer. Varying the lattice parameter \mathbf{a} in an interval of -5 % to + 5% around its theoretical value 7.718 au (according to

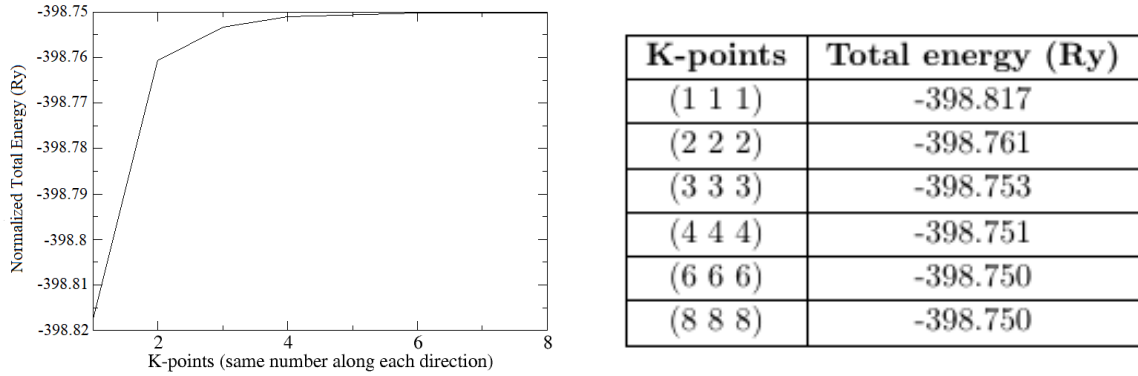


Figure 3.4: Primitive cell energy vs the number of k-points in the MP grid.

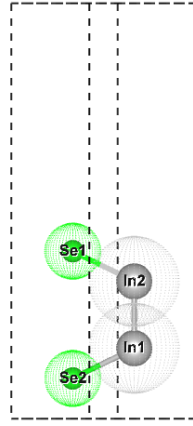


Figure 3.5: Representation of the unit cell of an InSe monolayer

reference [82]), we calculated the total energy as a function of \mathbf{a} . Notice that \mathbf{c} has been set to the constant value of $15.3772 \text{ \AA} = 29.059 \text{ au}$ (figure 3.5 shows the structure), large enough to avoid interaction between periodic replicas of the monolayer along the z direction of the supercell. The number of sampling k-points was kept constant to (6 6 1). These analysis have been carried out for four different cutoff energies (40 Ry, 45 Ry, 50 Ry and 55 Ry). Despite 45 Ry was found to be a good compromise between the computational cost and the accuracy of simulations for total energies, we double checked that the equilibrium structure is also converged at this cutoff. For each cutoff energy mentioned above, we performed eleven simulations at 11 different values of lattice parameters \mathbf{a} : the more stable is the structure, the lower is the energy, thus a minimum in the energy is expected when \mathbf{a} reaches its equilibrium value. Minima of the curves obtained from our calculations are close to the theoretical equilibrium lattice parameter \mathbf{a} . A comparison of the results is reported in figure 3.6.

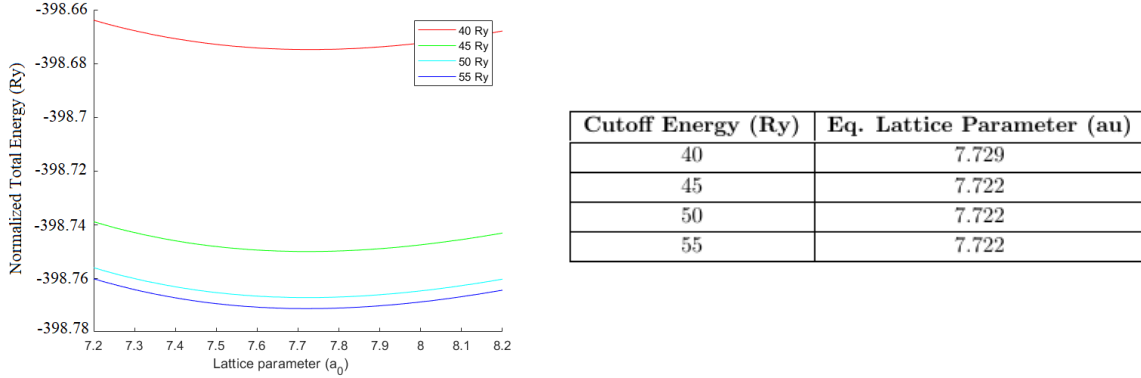


Figure 3.6: Comparison between the energy curves obtained for InSe monolayer at four different E_{Cutoff} (on the left) as a function of the lattice parameter. The right table report the values of the lattice parameter at equilibrium.

It is clear that for higher cutoffs, energies are more negative (this is in agreement with the Variational theorem) as shown in figure 3.6; however, it can be noticed that for the last three cases (45, 50 and 55 Ry) the difference in lattice parameter are within the calculation accuracy. These results confirm that a cutoff energy of 45 Ry gives converged results for InSe monolayer.

3.2.2 Band diagram

Once the optimal cutoff energy (along with its respective equilibrium lattice parameter) and the number of sampling k-points have been determined, we predicted the band structure of the material. These tests are very important because, by directly comparing our results with some reference articles, they can confirm once more the accuracy of our computational conditions.

Bands have been calculated under the convergence conditions evaluated so far (cutoff energy of 45 Ry, number of sampling k-points (6 6 1), $\mathbf{a}=7.722$ au ($\approx+0.05\%$ the reference value of 7.718 au, [82]), PBE ultrasoft (2.4.2) *scalar relativistic* pseudopotentials).

It can be noticed, in figure 3.7, the so called sombrero-shaped dispersion around the point Γ , which is given by the presence of two maxima around that k-value and an almost flat VB between them. This particular shape of energies vs k-points leads to the possibility for electrons to be easily transferred between energetically near states with a very small amount of thermal energy (i.e enhancement of the probability of electronic transitions between VB and CB). For this reason both the direct bandgap (evaluated in Γ) and the indirect one (calculated between one of the two maxima of the Valence Band and the minimum of the Conduction Band) have been found and reported here. Values of direct and indirect bandgaps are 1.24 eV and 1.08 eV, respectively. It can be noticed that these values represent an underestimation with respect to the reference article [87] (on the right) in which author used the Heyd-Scuseria-Ernzerhof (HSE06)

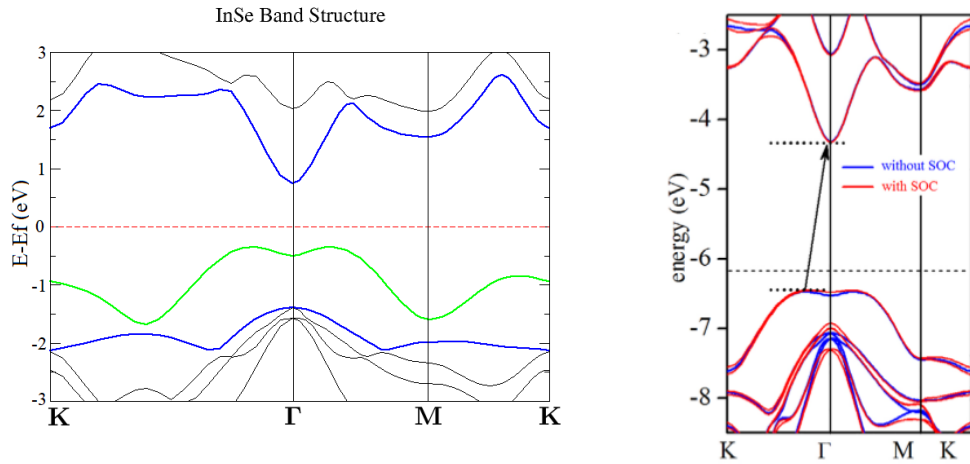


Figure 3.7: Comparison of the InSe band diagram obtained with our computational conditions (on the left) with the one reported in reference [87] (on the right). In the reference article we can also notice that the exploitation of the *Spin Orbit Coupling* does not imply any particular modification in the band dispersions.

hybrid functional and not the PBE one; this is a well known deficiency of DFT-PBE. Obtaining more accurate values of E_g one may use other techniques such as the already mentioned *HSE06* or the *GW0* [87], [73], however, as already discussed in section 1.4, their use would lead to a rigid shift of the dispersion relationship, without involving any substantial difference in the dispersion of the bands. This is apparent also in the comparison of the bands reported in figure 3.7. Inclusion of spin polarization in the DFT calculation does not improve the description of the dispersion relations as demonstrated by the comparison reported in figure 3.7 (on the right).

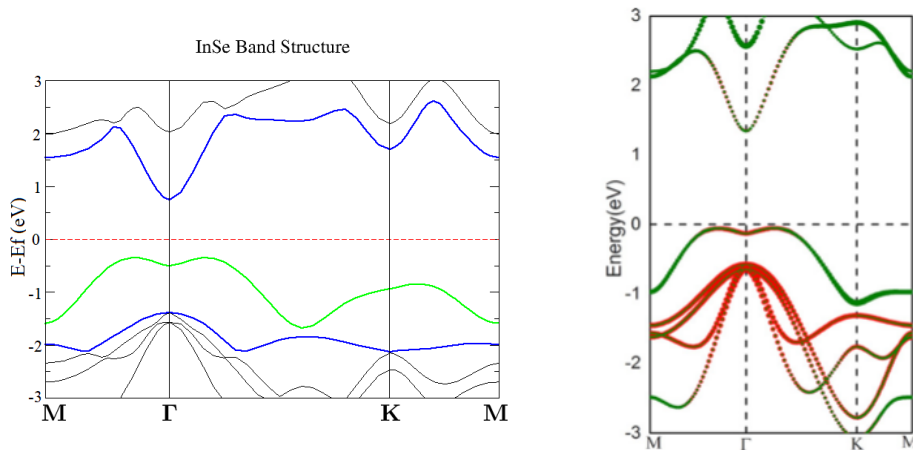


Figure 3.8: Comparison of the InSe monolayer band diagram obtained with our computational conditions (on the left) with the one of a reference article [80] (on the right).

3.2.3 Spin Orbit Coupling effect

Before proceeding we evaluated the impact of including the spin orbit coupling in the calculation of InSe properties. In particular we aimed at confirming the results reported in reference [73] and [87]. Author of these papers commented that the *Spin Orbit Coupling* (SOC) does not strongly effect InSe band structure as apparent from an analysis of figure 3.7 (from the reference [87]). To this purpose we repeated the above calculation reported in the first part of this chapter using relativistic pseudopotentials. Changing the pseudopotentials entails estimating again the converged PW cutoff energy and the equilibrium lattice parameter for InSe. Results are commented in the following paragraphs. As for the scalar relativistic pseudopotential case, the total energy of the primitive cell has been calculated for different cutoffs. Results are reported in 3.9. 20 and 30 Ry are definitely too small to guarantee a good approximation of the real world, while from 40 Ry onwards the convergence of energies is almost achieved. For

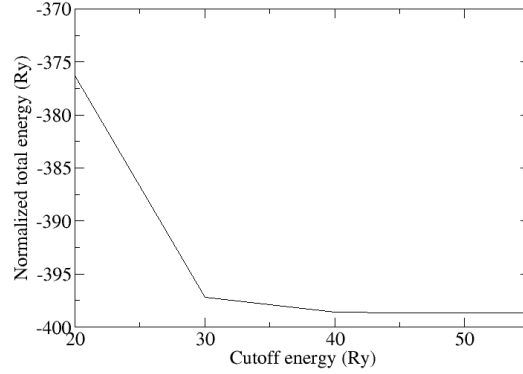


Figure 3.9: Primitive cell energies for different cutoffs with $\mathbf{a}=7.718$ au

four different PW cutoffs (40, 45, 50 and 55 Ry) the energy of the system has been evaluated as a function of the lattice parameter \mathbf{a} . Behaviours of the interpolating curves are practically identical with respect to the one obtained in the previous section (3.1.1), and no change in the equilibrium structure is observed including SOC explicitly. Moreover, according to our data

- $E(a)_{50} - E(a)_{45} \rightarrow \Delta E \approx 0.017 Ry$
- $E(a)_{55} - E(a)_{50} \rightarrow \Delta E \approx 0.004 Ry$

thus, also for the fully relativistic pseudopotentials employed in our calculations 45 Ry cutoff is sufficient to guarantee a converged results.

We finally report InSe monolayer band structure considering SOC and compare to the one obtained without including it (see figure 3.11). An analysis of the band dispersion highlights that the two band structures are very similar, particularly around the top of

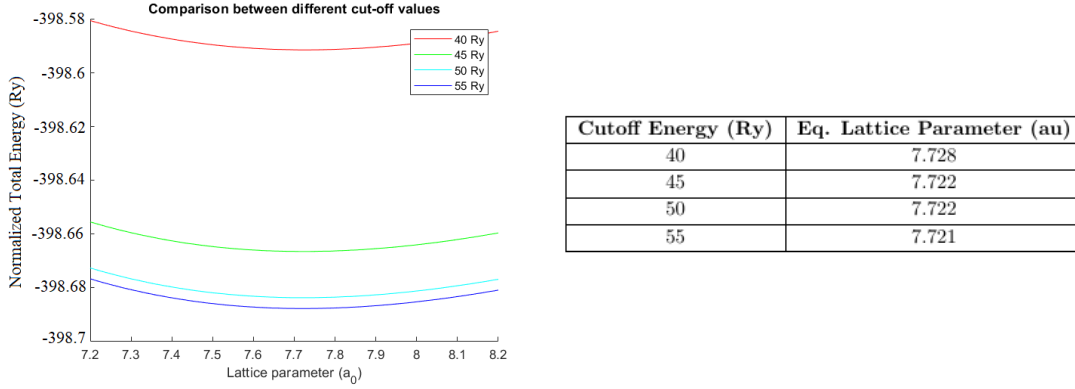


Figure 3.10: Energy curves obtained for the four different E_{CutOff} (on the left) as a function of InSe monolayer lattice parameter. The right table reports the values of the lattice parameters at the curve minima.

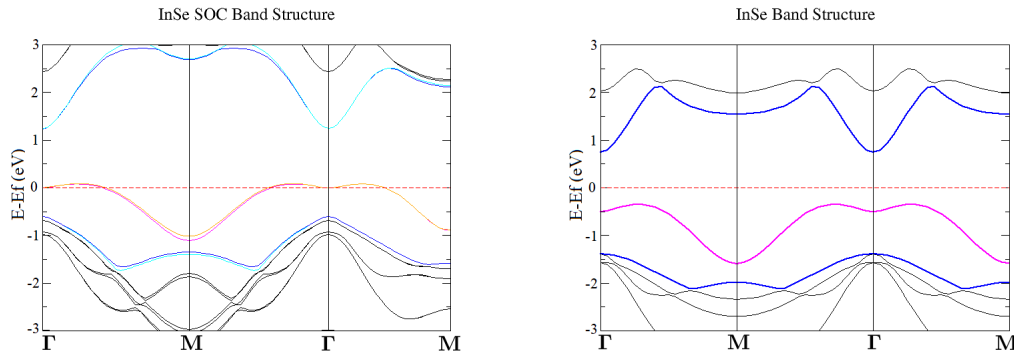


Figure 3.11: InSe monolayer band diagram obtained with (left panel) SOC and without (right panel) SOC

the valence band and the bottom of the conduction band, which is the most relevant part when interested in photo emission. There is a small difference in \mathbf{M} but at low energy levels which would not be involved into optical emission. Bandgaps are also very similar:

Bandgap	SOC	NO SOC
Direct	1.24 eV	1.24 eV
Indirect	1.15 eV	1.08 eV

These values are almost equal in the direct case, and $|\Delta E| \approx 0.07 eV$ in the indirect one, in agreement with what is reported in article [87]. Note that the direct bandgap has been evaluated at the Γ point.

In conclusion, considering the increase of the computational cost related to the use of *relativistic pseudopotentials* and in view of the negligible difference observed in the predicted properties of InSe monolayer when SOC is included, all results obtained

in this thesis work have been obtained without including spin-orbit coupling, being confident that this choice would not affect the accuracy of the calculations and the conclusion of our work.

3.3 Defects in 2D InSe: the supercell approach

According to what discussed in section 1.3, it is known that single photon emission can be obtained by the addition of impurities in crystalline systems which originate defect states in the band gap of the material. In this thesis work, we explore the possibility of obtaining SPE by means of doped InSe monolayer, predicting the electronic properties of this system when different type of impurities are introduced in the monolayer. The

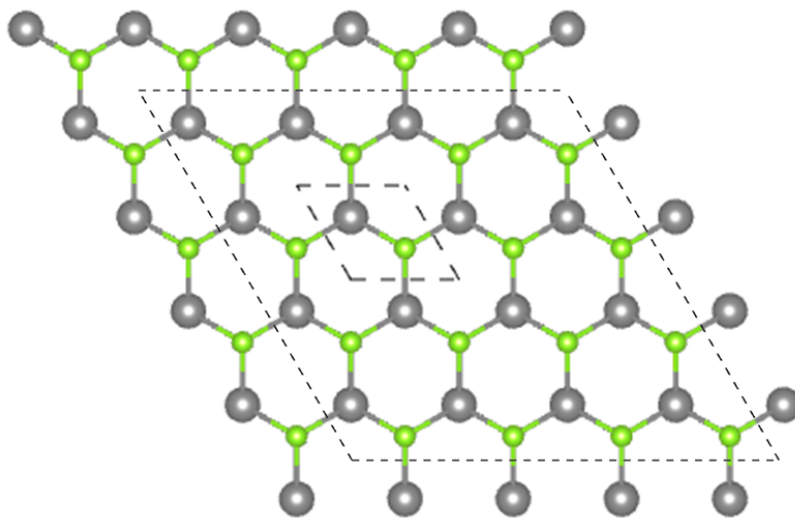


Figure 3.12: Here is reported the example of a 4x4 supercell. Notice the original unitary cell (highlighted in the center of the structure) and the new 4x4 supercell.

program used to perform the simulation is coded to deal with periodic systems, i.e. periodic boundary conditions are applied to the simulation cell. Indeed, the presence of impurities, breaks the periodicity of a lattice, yet it is possible to overcome this issue by employing the supercell approach (an example of supercell is shown in figure 3.12). Supercells allow to deal with aperiodic configurations of atoms within the framework of Bloch theorem, allowing to use a PW basis set. In this approach, to simulate a single impurity in an otherwise infinitely periodic lattice, one constructs a large unit cell containing a single impurity. In order to ensure that the results of the calculations accurately represent an isolated defect, the supercell must be large enough so that impurities of adjacent cells (replicas) do not interact with each other. Since the computational cost of the simulation increases as the supercell dimensions increase, a compromise must be reached between size of the cell and accuracy of the results. To

find the optimal size of the cell that satisfies this trade-off, one studies how the formation energy, E_{FORM} , and the electronic properties of a crystal with a chosen type of point defect, taken as reference, change as a function of the supercell size. In our case, we analyzed such dependence for a Selenium vacancy in InSe monolayer considering 2D supercells of increasing size, from a (2x2) to a (5x5) supercell (i.e. from 2 primitive cell replicas along x,y direction up to 5 replicas). By monitoring the variation of the vacancy formation energy (see 3.3.1) as a function of the dimensions of the system, together with the variation of the band structure, it is possible to determine the minimum supercell size which entails converged results. In practice in our calculations, we employed a cutoff energy of 45 Ry and built supercells with cell sizes corresponding to $n\mathbf{a}$, where n is the number of primitive cell replicas along the x and y directions and \mathbf{a} ($= 7.722 \text{ au}$) is the InSe equilibrium lattice parameter obtained at 45 Ry for a monolayer without defects. Because of BZ folding, when employing supercells, the MP grid used to sample the BZ can be reduced to a (2 2 1).

3.3.1 Selenium vacancy formation energy

Within the Density Functional Theory calculations, defects formation energy, E_{FORM} , can be obtained via total energies calculation of supercells containing single defects. In particular for InSe monolayer E_{FORM} can be defined as follows:

$$E_{FORM}[X] = E_{TOT}[X] - E_0 + n_{In}\mu_{In} + n_{Se}\mu_{Se} - \sum_X n_X\mu_X \quad (3.1)$$

Where E_0 is the total energy of the pristine supercell (i.e. without any defect) provided by $E_0 = n\mu_{InSe}$ (n is the total number of InSe pairs in the supercell and μ_{InSe} is the chemical potential of the InSe stable phase); $E_{TOT}[X]$ is the energy of the defect containing supercell. In the case of substitutional impurities, X indicates the atomic species introduced in the InSe layer while n_X is the number of X atoms added to the system. n_{Se} and n_{In} are the number of Se and In atoms removed from the layer and substituted by X species, while μ_{Se} and μ_{In} are the chemical potentials of selenium and indium, respectively, in their stable bulk phases. In the specific case of a selenium vacancy, that we took as reference system to determine the required supercell size to obtain converged results, equation 3.1 can be simplified because the structure is obtained by simply removing one Se atom from the supercell; therefore n_X and n_{In} are null and $n_{Se} = 1$. E_{FORM} can be then rewritten as:

$$E_{FORM} = E_{TOT} - E_0 - \mu_{Se} \quad (3.2)$$

It can be noticed in table 3.3.1 that the formation energies do not show large differences and the change in E_{FORM} passing from a 4x4 to a 5x5 supercell is $\Delta E = 0.03 \text{ eV}$ only. For a more clear conclusion on the required supercell size to study isolated defects, we thus analyzed and compared the electronic properties of the defected systems. This comparison is discussed in the following paragraph.

Supercell	E_{FORM} (eV)
2x2	2.23
3x3	2.22
4x4	2.16
5x5	2.13

Table 3.1: Here is reported the formation energy of the Se vacancy as a function of the dimension of the supercell. We can notice that this value does not undergo to any substantial modifications passing from a 2x2 to a 5x5 supercell since $\Delta E \approx 0.1eV$ only.

3.3.2 Selenium vacancy electronic properties

The presence of insulated vacancies in a semiconductor should lead to the formation of well defined energy states in the band diagram of the material, showing no dispersion. However, since we are simulating defects in supercells, which are periodic systems, if the cell is not large enough, defects will interact with their periodic images and this interaction will give raise to defects state showing large dispersion in the BZ. This is an artifact of the simulation which has to be avoided if one is interested in understanding the electronic effects of isolated (or diluted) defects. To identify the supercell size required to represent isolated defects one can analyze how the band diagram and the Density of States (DOS) of the system changes by changing supercell. In our case for each supercell discussed in the previous paragraph containing a Selenium vacancy, the DOS (Density Of States) and the Band Diagram are reported in figure 3.13, 3.14, 3.15 and 3.16 (note that the Fermi level has been set to 0).

As it is apparent from figure 3.13, the 2x2 supercell is too small to represent isolated vacancies. Indeed, the DOS shows a dispersion in energy of the new state (fact that leads to a bent energy level in the band diagram), while the result one expects is a sort of Delta-like behaviour. Despite the evident inadequacy of the supercell, here a quantitative analysis of the situation has been reported: *direct distance* $VB=0.76$ eV (this is the distance in energy measured between the defect energy level and the VB in the Γ point); *indirect distance* $VB=0.34$ eV (energy difference between the minimum of the defect energy level and the maximum of the VB); *direct distance* $CB=1.55$ eV (distance in energy between the CB and the defect energy level in Γ); *indirect distance* $CB=0.29$ eV (energy difference between the minimum of the CB and the maximum of the defect energy level). Despite the small dimensions, one important consideration can be made: looking at the number of valence electrons in the system (216, given as output in our simulations) and knowing that the energy state within the gap is the 108-th band one discovers that the presence of a vacancy in the lattice generates a *donor level* in the gap (i.e. 2 electrons within the energy level). This assumption is obviously valid also for the bigger structures which owns a single Se vacancy. For what concerns the PDOS (not reported here), instead, one should highlight that in the

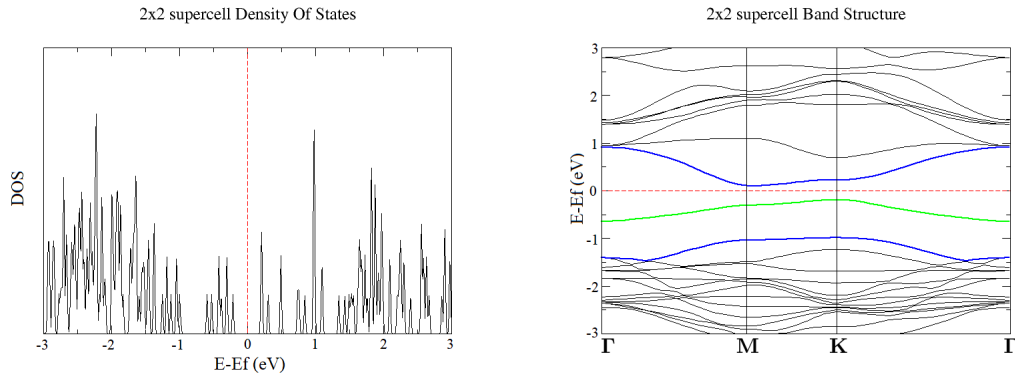


Figure 3.13: Total DOS and Band Structure in the case of a 2x2 supercell; the green level is generated by the presence of the Se vacancy, but it is not flat

VB the Se gives the more relevant contribution to the occupied states, while In atoms acquire more importance in the CB.

As in the previous case, the small dimension of the structure leads to a dispersion in energy of the DOS. Despite the "thickness" of this dispersal is thinner than in a 2x2 supercell, results are not acceptable for the study of defects (see figure (3.14)). In the following a quantitative analysis has been reported: *direct distance VB*=0.45 eV; *indirect distance VB*=0.18 eV; *direct distance CB*=1.44 eV; *indirect distance CB*=0.77 eV. The flatness of the donor level starts to be more evident, however it can be further

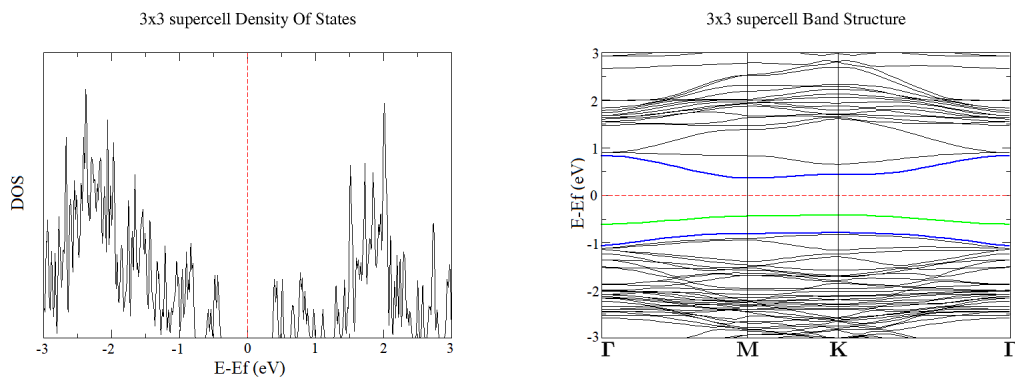


Figure 3.14: Total DOS and Band Structure in the case of a 3x3 supercell; the defect cannot be considered insulated since the green band is still not flat

improved exploiting larger structures. No other noticeable differences with respect to the previous case are present.

The 4×4 and 5×5 supercells represent a decisive improvement of the model. Considering the two figures 3.15 and 3.16 as references for the 4×4 and the 5×5 cases, respectively, the flatness of the donor levels in the two band structures and the be-

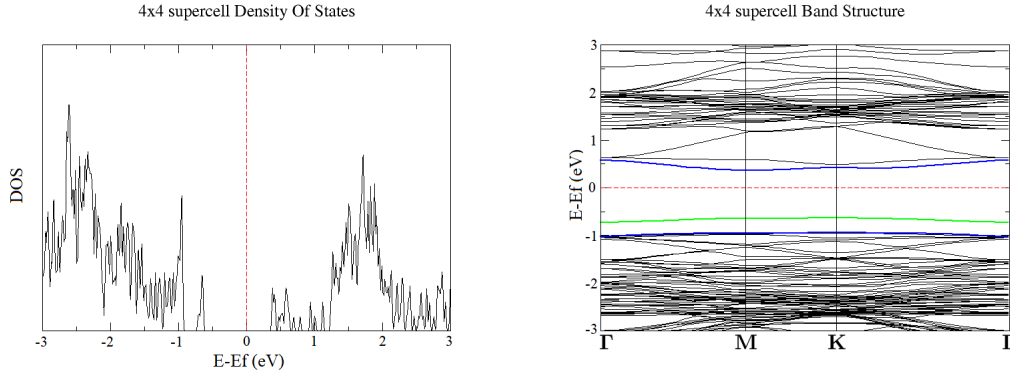


Figure 3.15: Total DOS and Band Structure of the defected 4x4 supercell; the influence of the image of the defect on the defect is extremely weak and the green energy state is flat

Energy distances	4x4	5x5
Direct distance VB	0.30 eV	0.27 eV
Indirect distance VB	0.22 eV	0.25 eV
Direct distance CB	1.30 eV	1.21 eV
Indirect distance CB	1.00 eV	1.10 eV

Table 3.2: Energy distances calculated for the 4x4 and the 5x5 supercells.

haviours of the densities of states are clearly similar. In table 3.2 are reported the distances in energy between the different levels both for the 4x4 and the 5x5 cases.

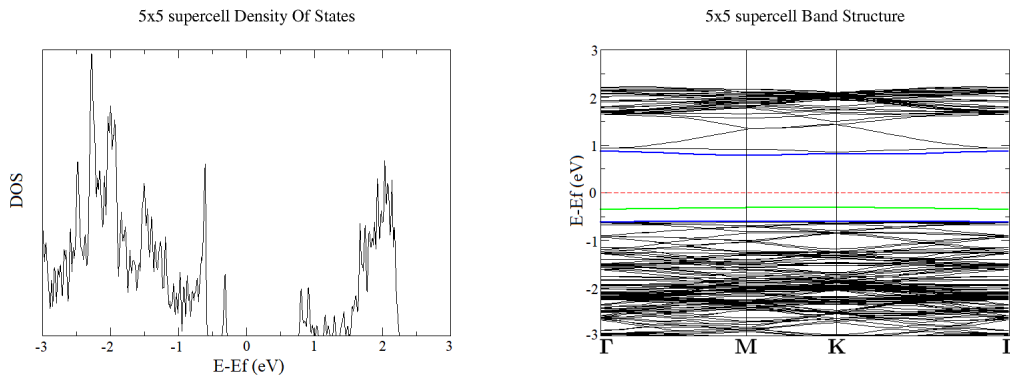


Figure 3.16: Total DOS and Band Structure of the 5x5 supercell; in this case the defect can be considered perfectly insulated from its periodic images

According to the DOS, it can be noticed that dispersions of the occupied states within the bandgap are Delta like in both cases, indeed their "thicknesses" are 0.089 eV and 0.034 eV for the 4x4 and the 5x5 structures, respectively, meaning that they differ

only by 0.05 eV. Furthermore, values of energy differences of table 3.2 are converging and also the formation energies reported in table 3.3.1 are almost identical. All these considerations suggest that both the systems are well suited to model an insulated defect. Nevertheless, since results are very similar, but the computational cost of the 5x5 structure is very expensive compared to the other case, the 4x4 supercell has been chosen to perform the analysis of defects. A more complete discussion on the presence of a vacancy in the lattice, however, is reported in the next chapter.

CHAPTER 4

Study of vacancies and substitutional impurities in InSe monolayer

In the last section of the previous Chapter, we have shown that the presence of a vacancy in the InSe monolayer leads to the formation of an extremely narrow energy state within the bandgap of the material. In this chapter the effect of other defects (substitutional impurities) will be presented, with the aim of understanding if doping of InSe monolayer can be used as an effective way to induce single photon emission behavior. For each type of impurity considered here, we analyze the modifications induced in the electronic properties of an InSe monolayer in terms of Band Diagram, Density Of States (DOS), and Projected Density Of States (PDOS). In addition, for the most interesting systems, we also analyzed the spatial localization of the defect state beside calculating the energy difference between the defect state and the Fermi energy of the system, $\Delta E^d = E_{defect} - E_{Fermi}$. Further, for all systems we calculated the energy of the highest occupied state (E^{HO}), the energy of the lowest unoccupied state (E^{LU}), relative to the Fermi level, and their difference $\Delta E^{LU,HO} = E^{LU} - E^{HO}$. This analysis allowed us to identify the presence of low dispersion defect states in doped InSe monolayer, which is a prerequisite to generate SPE. Thermodynamic stability of doped systems has been addressed by calculating the defects formation energies defined in section 3.3.1 which, for all studies cases, are summarized in table 4.1.

In addition to Se vacancies and to the substitutional impurities discussed in sections 4.1, 4.2, 4.3 and 4.4, in this thesis work we studied the substitution of Ga in place of In atoms. The latter systems are discussed in details in the next chapter (5).

4.1 Se vacancy defect

We here first discuss more in details the effects induced in InSe by a Se vacancy, which has been already introduced in section 3.3.2. The formation energy required to generate this kind of defect is slightly larger than 2 eV, thus vacancies are likely to be easily

Defect	E_{FORM} (eV)
O_{Se}	-1.46
S_{Se}	-0.04
Ga_{In}	-0.05
Ge_{In}	1.34
Ge_{Se}	2.61
N_{Se}	2.95
P_{Se}	1.81
As_{Se}	1.69
Se vacancy	2.16

Table 4.1: Formation energies for different type of substitutional impurities in InSe monolayer.

formed with common technological approaches. The band diagram of InSe containing a vacancy defect is reported in figure 4.1; it is possible to notice that the Fermi level (the dashed red line) is well above the defect state (green line), meaning that a Se vacancy induces the presence of a donor level (i.e. a fully occupied defect band). At first look, considering the total PDOS of figure 4.1, this level seems to be given only by the contribution of the Se orbitals; however, observing carefully the density of states projected on Se and In species (see figure 4.2), it is clear that both Se and In atoms contribute to this state. Indeed, both the projections present a peak around the same energy value ($\approx -0.6eV$ with respect to the Fermi level which is set as reference energy to 0 eV) indicating that their contributions are equally important. In addition, we can say that the upper valence band has predominantly a Se-p character with some hybridization with In-p orbitals, while the lower conduction band has mainly In-s and In-p character even if we can clearly distinguish also the presence of Se-p orbitals. Since the presence of a Se vacancy in InSe monolayer leads to the formation of a well defined state within its bandgap, we also analyzed the spatial localization of this new level. To this aim, we have calculated and represented (in figure 4.3) the electron density corresponding to the defect state. It is clearly visible that the density is concentrated around the Se vacancy and, in particular, we can notice that it is equally distributed around all surrounding atoms (i.e. both Se and In). This is in agreement with the PDOS analysis reported above. In this structure, the energy of the highest occupied state coincides with E_{defect} and, in particular, $E^{HO} = \Delta E^d \approx -0.64eV$. For what concerns the lowest unoccupied state, instead, we have $E^{LU} \approx 0.36eV$ (which coincides with the conduction band minimum, CBm) and the resulting $\Delta E^{LU,HO}$ corresponds approximately to 1 eV.

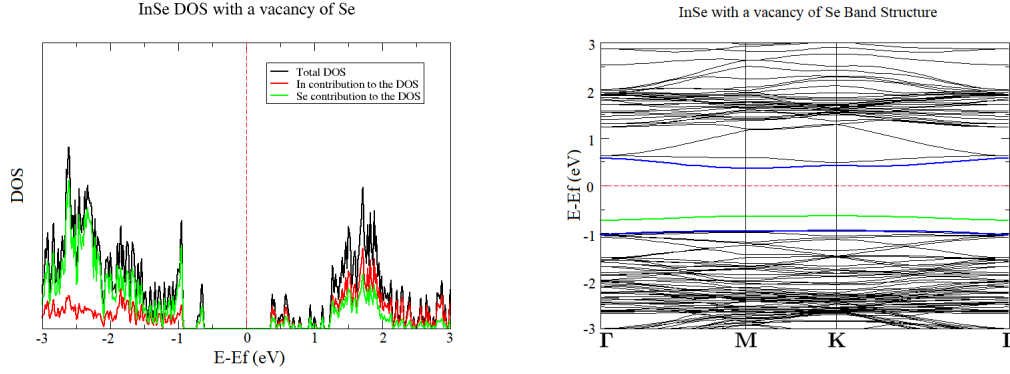


Figure 4.1: PDOS and Band Structure of InSe with Se vacancy. On the left the PDOS shows that the upper valence band has predominantly Se-orbitals character, while the lower CB is the result of both In and Se contributions; on the right we highlighted the top most level of the VB, the defect state (in green), the bottom of the CB, and the Fermi level (the dashed red line).

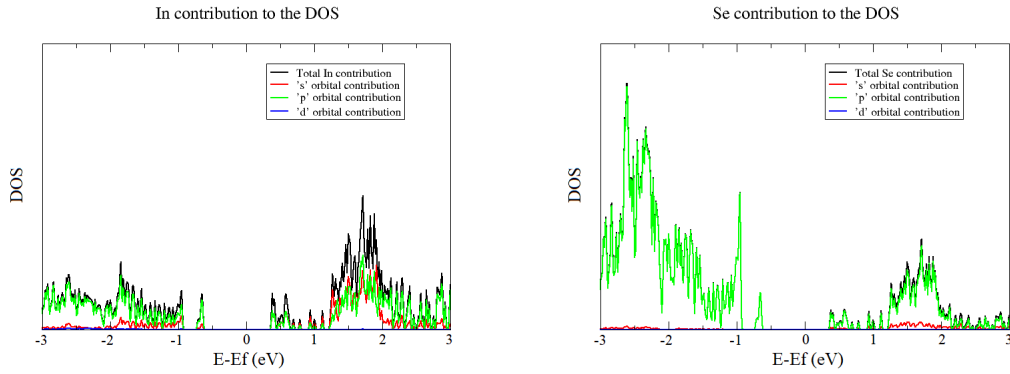


Figure 4.2: Projected density of states related to In, on the left, and Se, on the right. Se contribution has a p-orbital character, while for what concerns the In case, both s and p orbitals are relevant (especially in the conduction band).

4.2 Group VI substitutional impurities: O and S

According to the literature (see e.g reference [77] and [78]), the presence of oxygen impurities in InSe monolayer can be quite frequent due to the fabrication processes exploited to produce the material and the intrinsic sensitivity of InSe to the presence of air. For this reason, we calculated how this impurity affects the electronic properties of InSe, substituting Se with O atoms. In the case of oxygen the defect formation energy is negative (see table 3.3.1), confirming the tendency observed experimentally of InSe to spontaneously incorporate oxygen when exposed to air. Analysing the band structure and the density of states reported in figure 4.4 for O containing InSe and

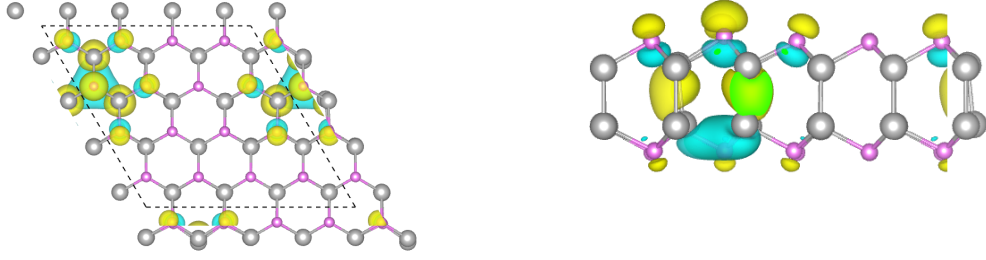


Figure 4.3: Isosurface plot of the electron density related to the defect energy state, which also correspond to the highest occupied state of the system. The electron density is mostly localized nearby the Se vacancy.

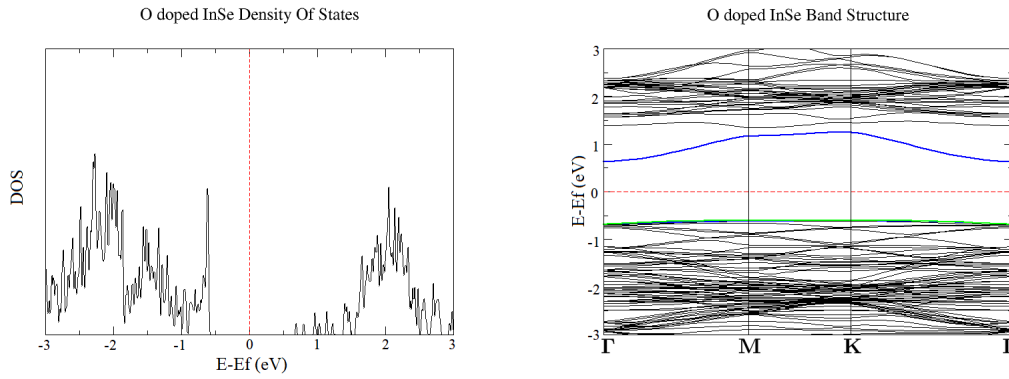


Figure 4.4: DOS and Band Structure of the InSe monolayer with a substitutional impurity of oxygen in place of a Se atom. The defect state is fused with the upper valence band.

comparing the graphs with those obtained for the case of InSe with vacancy point defects, it can be noticed that oxygen substitutional impurity leads to defects states degenerate with InSe states at the top of the valence band (VB). This is an indication that the bond between O and the nearby In atoms is somewhat similar to that of In-Se bonds, thus resulting in energy levels within the InSe VB. Oxygen does not generate defect states useful for single photon emission, still since it mainly alter InSe density of states in the valence band energy range, even when present as residual impurity after InSe growth, it would not have detrimental effects on InSe optical properties. For the sake of comparison, we have studied the effect of another group VI element, namely sulfur, when present in InSe as an impurity substituting Se atoms (note that Se, O and S belong to the same group of the periodic table). Similarly to O substitutional impurities, also substitution of Se with S is characterized by negative formation energy, thus substitution of Se with S leads to a thermodynamically stable system (negative formation energy). Moreover, comparing the band structure of InSe with a S impurity

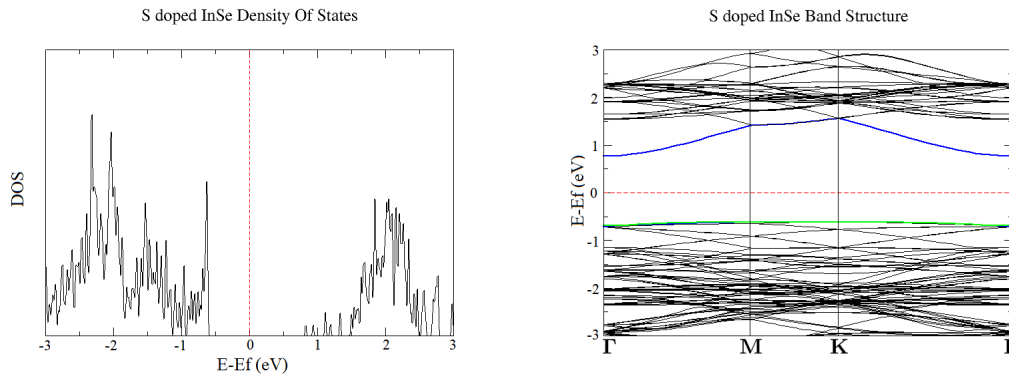


Figure 4.5: DOS and Band Structure of the InSe monolayer with a substitutional impurity of sulfur in place of a Se atom. The defect state is fused with the upper valence band.

(figure 4.5) with the band structure of InSe with an O impurity (figure 4.4) the main electronic features appear to be similar. Also sulfur does not lead to the formation of distinct energy states in the gap, but gives rise to defect levels degenerate with the top of InSe valence band.

4.3 Group V substitutional impurities: N, P and As

We here consider the electronic effects of group V impurities in InSe, namely nitrogen, phosphorus and arsenic substituting selenium atoms. Formation energies listed in table 4.1 clearly indicate that those defects can be generated without any technological issue since E_{form} values are similar to the one obtained for selenium vacancies. For the case of N doping, we reported the DOS, the band diagram, the projected density of states and the HOMO in figures 4.6, 4.7 and 4.8, respectively. For what concerns phosphorous and arsenic impurities, instead, we reported the band diagrams (figure 4.9) and the PDOS (figure 4.10), since the other analysis do not provide additional information with respect to what observed for the N substitutional impurity. Analysing the N:InSe band diagram, in particular, one can notice that the energy level associated to the presence of N within the bands gap can work both as a donor or as an acceptor state since it is only half filled (the Fermi level lies at the defect state energy). Analysing the spatial distribution of the electrons associated to the energy state observed within the gap (4.7), it is clear that this state is localized around the N atom, and, in this case, first neighbours give a smaller contribution compared to the case of the selenium vacancy. Figure 4.8 shows, instead, the contribution of the N atom to the density of states. It can be seen that N contribution to the VB and CB is almost negligible, while

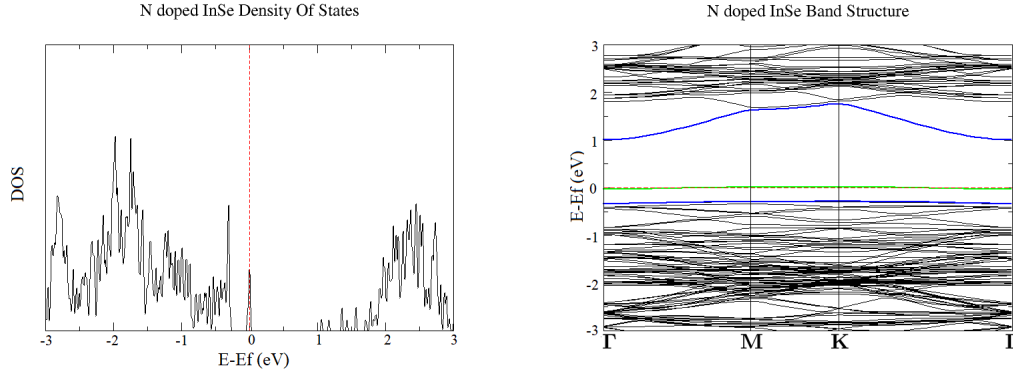


Figure 4.6: DOS and Band Structure of the N doped InSe. A defect energy state (yellow line) appears within InSe bandgap very close to the top of the VB.

it is extremely relevant for the state observed within the bandgap (its contribution derives almost completely from p orbitals). The value of ΔE^d is null because the

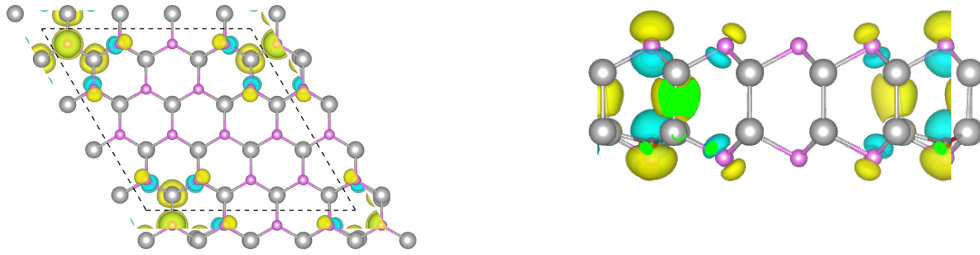


Figure 4.7: Molecular orbital associated N substitutional impurity in InSe.

defect state coincides with the Fermi level and also $E^{HO} = E_{defect}$ is zero since it is defined with respect to E_{Fermi} . E_{LU} , instead, coincides with the CB minimum and $\Delta E^{LU,HO} \approx 1.00eV$. Since we are dealing with a level that can also accept an electron, it is useful to define another parameter $\Delta E^{HO,VB M}$ which is given by $E^{HO} - E^{VB M}$; in this case $\Delta E^{HO,VB M} \approx 0.30eV$. In the table 4.15, we report these parameters for phosphorous and arsenic impurities too.

4.4 Group IV substitutional impurities: Ge

Of the group IV of the periodic table we considered the effect of Ge impurity only, analysing the modifications induced in InSe both as In and Se substitutional defect. Since Ge has one more electron than In and one less electron than Se, it may generate both donor and acceptor states depending on the position of the defect within the lattice.

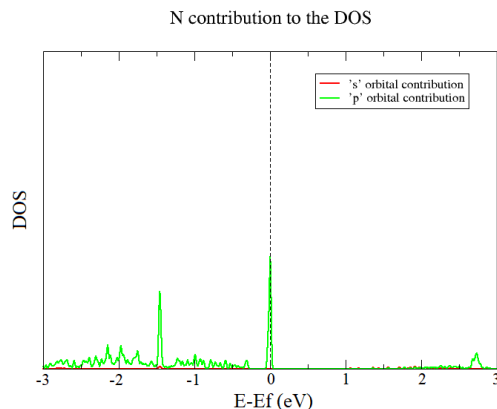


Figure 4.8: N contribution to the DOS. In this energy range the density of states is determined by N-p orbitals.

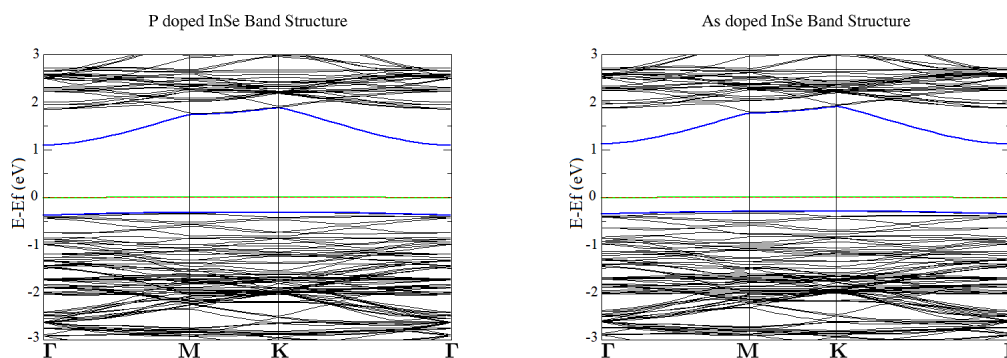


Figure 4.9: Band Structures of InSe monolayer with P (on the left) and As (on the right) substitutional impurities. An energy state (green line) which can work both as an acceptor and as a donor level appears in correspondence of the Fermi level in both the cases. The flatness of the two states makes them suitable to be employed as single photon sources.

In figure 4.11, we report the band structure and the DOS of InSe with one Ge atom in place of one In. The substitutional defect leads to the formation of a well defined energy state within the bandgap. It is possible to see that the Fermi level intersects this the defect state (similarly to what happens for the V group substitutional impurities) which indeed is half filled, and thus can work both as a donor or an acceptor state. However, despite the formation of this impurity is one of the most energetically favourable (according to values in table 3.3.1) and the position of its related state is within the bandgap, observing the DOS, the dispersion of the defect level is too wide to work as a single photon source.

For what concerns Ge impurity substituting Se results are shown in 4.12. E_{FORM}

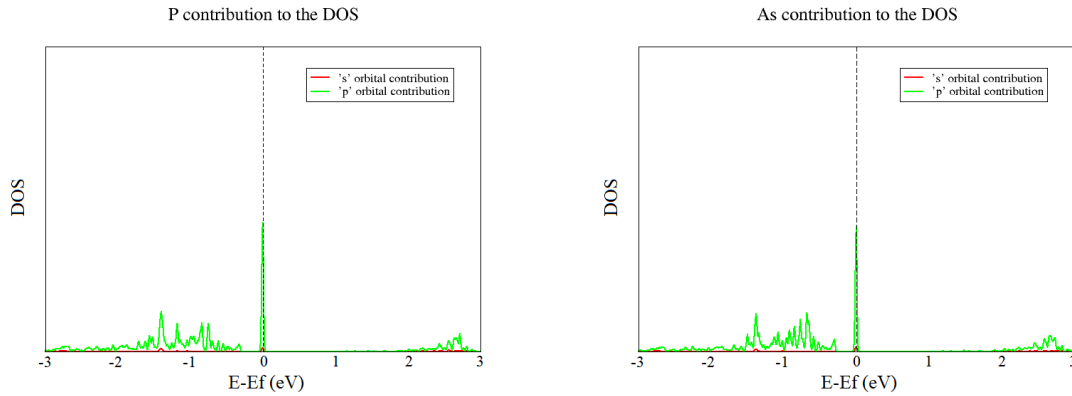


Figure 4.10: In this picture we can see that in both cases the defect state is almost totally characterized by the Se-substitution 'p' orbitals, in agreement with all the other cases.

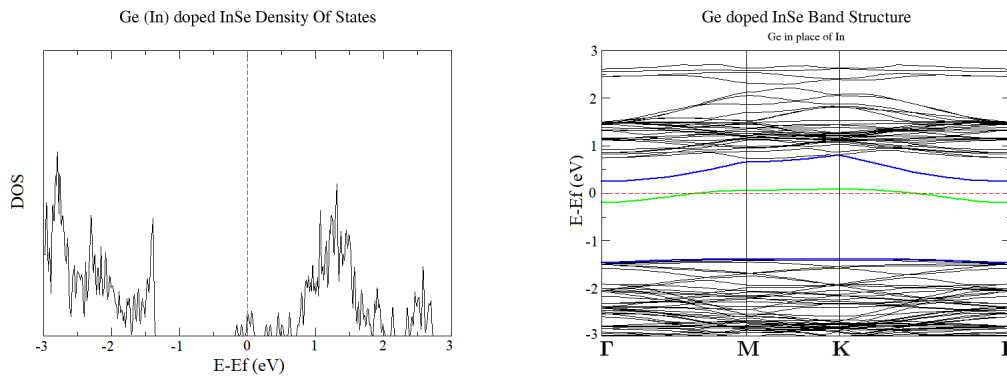


Figure 4.11: DOS and Band Structure of Ge doped InSe (Ge in replacing In).

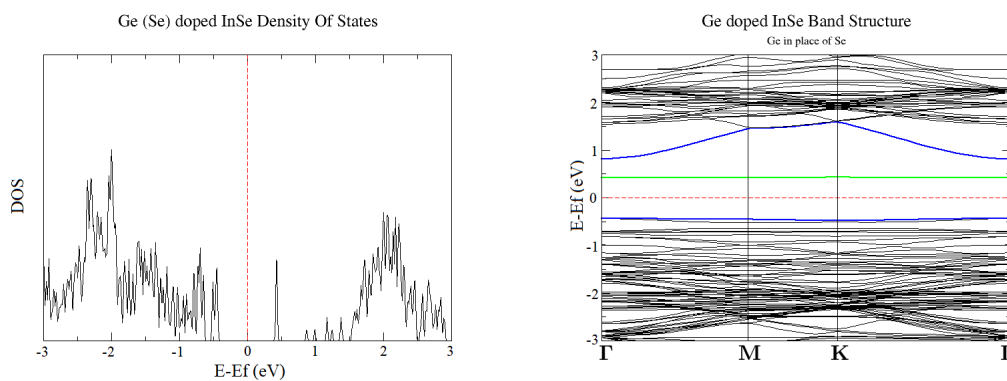


Figure 4.12: DOS and Band Structure of the Ge doped InSe (Ge is replacing Se).

is one of the largest obtained among the impurity species considered in this thesis

work, but still within a range of technologically achievable doping. The DOS presents an extremely narrow peak which results in an almost perfectly flat defect level in the dispersion relationship. Contrarily to what happens in the Se vacancy or in N, P and As defect cases, the state originated by Ge is closer to the CB and well above the Fermi level thus it is an acceptor state (or LUMO state), therefore, according to the notation introduced previously, $E_{defect} = E^{LU} = \Delta E^d \approx 0.42eV$. The energy value of the highest occupied level, always referred to E_{Fermi} , is instead $E^{HO} \approx -0.44eV$ (although the upper valence band is almost flat we have considered the valence band maximum VBM as E^{HO}) and the resulting energy difference between the HOMO and the LUMO is $\Delta E^{LU,HO} \approx 0.86eV$. Image 4.13 represents the electron localization corresponding to the wavefunction associated to the energy level within the bandgap. It is clear that this state is localized around the germanium atom (represented in figure by the red dot) since the modulus square of the wavefunction is concentrated around the defect. This localization is greater than in the case of Se vacancy and of V group defects since only a very small contribution comes from the neighbour atoms. In the figure 4.14, it

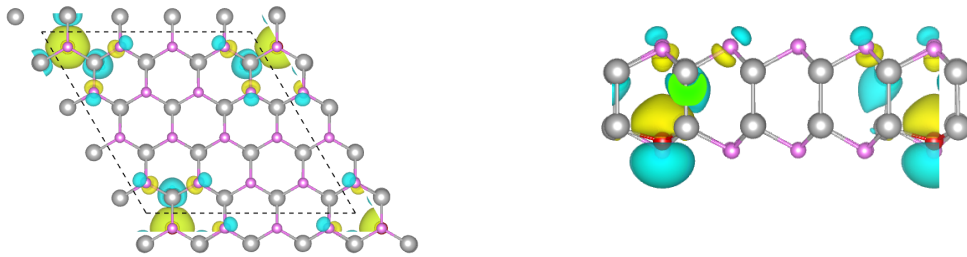


Figure 4.13: In this figure we have shown the molecular orbital associated to the defect energy state generated by the substitutional impurity if Ge (in place of Se). In this case this is a LUMO since we are dealing with an acceptor level.

is possible to directly evaluate the contribution of the Ge atom to the density of states. One can see that, similarly to the cases analyzed in the previous section, it is almost negligible in the VB and CB, but it is dominant within the bandgap. The defect state, in particular, has an evident Ge-p orbitals character while s and d one are not relevant.

4.5 Final discussion of impurity defects in InSe

In conclusion, we have shown that VI-group-element substitutions (i.e. O and S) of Se behave differently from V-group-element (N, P and As) and Ge substitutions of selenium in terms of electronic structure. Group IV elements, indeed, do not provide useful results for the single photon emission application since the presence of these defects

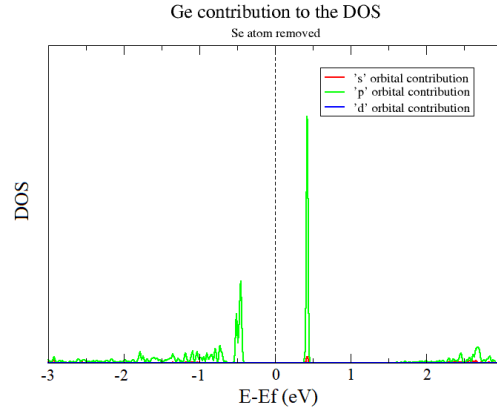


Figure 4.14: Ge contribution to the DOS when substituting Se in an InSe monolayer. p orbitals give the main contribution to the density of states of the lowest unoccupied state.

simply results in an increase of energy levels degenerate with the VB. On the contrary, when a defect belonging to the V group are considered, we can observe an extremely flat band well distinct from the valence band which is ideal to generate SPE. The difference arises from the bond characters between selenium-substitute (Se_X) and In or indium-substitute (In_X) and Se (in the case of Ge doping). If bonds are similar to In-Se bonds, the band structure does not undergo to any substantial modification, while if they differ from the chemical bonds of the pristine layer, some relevant differences may appear. A rough indicator of the bond character can be found in the electronegativity χ : in the case of VI-group-element or Ga substitutions the difference between electronegativity of Se (2.55) and S (2.58), indeed, is very small, and the same consideration can be done for χ_{In} (1.78) and χ_{Ga} (1.81), meaning that $\chi_S - \chi_{In} \approx \chi_{Se} - \chi_{In} \approx \chi_{Se} - \chi_{Ga}$. This results, therefore, in a simple variation of the DOS in the upper VB without the generation of any states within the bandgap. In the case of N, P, As and Ge substitutions, instead, considering the electronegativity values of Ge (2.01), N (3.04), P (2.19) and As (2.18) we can notice that they are quite different from the one of Se and In. As a consequence, bonds between Se-substitute and In are characterized by a $\Delta\chi$ which is well different from the one that marks the pristine In-Se bond. Thank to this fact we can assist to the destabilization of energy levels which are therefore well separated from the valence band.

As for the defect formation energies, it can be noticed that O-defect formation energy is very negative and this confirms the InSe sensitivity to air, which indeed tends to incorporate this atom in its lattice, also sulfur impurity is thermodynamically favoured but unfortunately it does not provide any interesting system to be exploited as SPE. Excluding these two cases, the most energetically favoured defect appears to be Ge_{In} which, however, exposes a wide defect state that limits its employment in

our applications. For what concerns the doped systems promising for SPE, we can notice that, in general, formation energy decreases moving down along the V group, so that $As_{Se} < P_{Se} < N_{Se}$, while for Ge_{Se} and Se vacancy they are slightly smaller than $E^f[N_{Se}]$ and quite bigger than $E^f[P_{Se}]$, respectively.

In table 4.15, we have reported electronic structures of the systems analyzed previously. We can observe that $\Delta E^{LU,HO}$ values are dependent on the type of impurity considered; in the case of V group defects, in particular, there is an increase of this quantity when moving down along the group of the periodic table, this behaviour is opposite with respect to the one of E_{FORM} . For what concerns types of electronic transitions (reported in the last column) we should highlight that in the cases of N, P and As we have labelled the defect level E_{defect} with LU when it works as an acceptor state, and with HO when instead it donates its electron to the CB minimum.

Defect	E^{HO}	E^{LU}	$\Delta E^{LU,HO}$	$\Delta E^{HO,VBM}$	ΔE^d	Transition
Ge (Se)	-0.44 eV	0.42 eV	0.86 eV	/	0.42 eV	VBM \rightarrow LU
N	-	1.00 eV	1.00 eV	0.30 eV	-	VBM \rightarrow LU/HO \rightarrow CBm
P	-	1.09 eV	1.09 eV	0.32 eV	-	VBM \rightarrow LU/HO \rightarrow CBm
As	-	1.13 eV	1.13 eV	0.28 eV	-	VBM \rightarrow LU/HO \rightarrow CBm
Se vacancy	-0.64 eV	0.36 eV	1.00 eV	/	-0.64 eV	HO \rightarrow CBm

Figure 4.15: E^{HO} and E^{LU} are the energies of the highest occupied and lowest unoccupied states, respectively, while $\Delta E^{LU,HO}$ is their difference. ΔE^d represents instead the energy positions of defect states provided by $E_{defect} - E_{Fermi}$. To conclude, in the last column we have reported the type of electronic transition.

In conclusion, in this chapter we have analyzed the energetic and electronic properties of point defects in InSe obtained through the substitution of a selenium or of an indium atom with one belonging to the III (Ga), IV (Ge), V (N, P, As) or VI (O, S) group of the periodic table. Despite the computed formation energies show that defects obtained through the exploitation of Ga, S and O are generally more favorable than the one obtained for Ge, N, P and As substitutions, our study of the electronic properties indicates that they do not introduce well defined defect energy levels within the InSe bandgap, rather in these cases these states tend to fall within the valence band. On the contrary, N, P, As and Ge substitutions of Se, along with the selenium vacancy, generate defect levels that are well distinct both from the VB and the CB of InSe; in particular, states emerging from the presence of Ge are shallower, while for V group atom substitutions and Se vacancy, they are deep in the bandgap. These states allow for new electronic transitions between the HO defect state and CB minimum (in the case of selenium vacancy) and between the VBM and the LU defect state (for Ge); when we introduce N, P or As impurities, instead, we can exploit both of these new transitions since the defect state can act both as donor and as acceptor. In conclusion, our results highlight that the proposed Se-substitutions in InSe, along with the

selenium vacancy, can be attractive for SPE since the depth of defect levels guarantee their thermal stabilities, they possess strong spatial localization and their formation energies are non prohibitive for their employment.

CHAPTER 5

Properties of $In_{1-x}Ga_xSe$ alloys

As already mentioned in the previous chapter, we have also studied the substitutional defect of a Ga atom in place of an In one. Similarly to what obtained for oxygen and sulfur (4.2), this lattice modification do not leads to defects state in the gap of indium selenide, however, due to the promising characteristics shared by InSe and GaSe (briefly discussed below) we have studied in depth the properties of $In_{1-x}Ga_xSe$ alloys as possible materials to be used as single-photon emitter.

InSe and GaSe have shown excellent optoelectronic properties and potential photonic applications [106], [86], [107], they possess almost lattice-matched films and thickness-dependent, tunable bandgaps [108], [109], [110] which are direct in bulk form and quasi-direct in the monolayer phase [79], [111]. Considering all the common characteristics listed so far, we have therefore predicted the phase diagram of $In_{1-x}Ga_xSe$ by varying the alloy composition and investigated its electronic properties and its possible exploitation as SPE for different In/Ga fractions. To this aim we employed the Cluster Expansion method (CE) combined with DFT calculations (see section 2.5 for the detailed explanation of the process).

5.1 $In_{1-x}Ga_xSe$ phase diagram

The Cluster Expansion is a method used to predict alloy stability and concentration dependent phase diagrams. From a practical point of view, the construction of a phase diagram for the alloy is a step by step process that involves alternatively one DFT (which provides a new energy E_n to add a new equation to the system 2.39) and one Cluster Expansion (which consists in the calculation of a new coefficient J_n for the expansion 2.38) calculation. This operation is carried out until one reaches an accuracy threshold for the ECIs which is monitored by the cross-validation score parameter: when this one becomes smaller than $k_B T$ (that is $\approx 25meV$ at room T) it means that coefficients of the expansion are reliable and the procedure can be interrupted. Since at the beginning of the simulation one has to provide the structures of the two

pure phases (i.e. InSe, already obtained, and GaSe), our first task was to determine the equilibrium structure of GaSe monolayer. The accuracy tests performed for GaSe were similar to the one reported in chapter 3 thus only main results are reported here. A cutoff energy of 45 Ry and a number of sampling k-point equal to $(6 \ 6 \ 1)$ have been found to be appropriate also for the study of GaSe. In these conditions the predicted equilibrium lattice parameter \mathbf{a} is 7.221 au (i.e. 3.821 \AA). GaSe monolayer band structure was compared to that of InSe and reported in figure 5.1. It can be

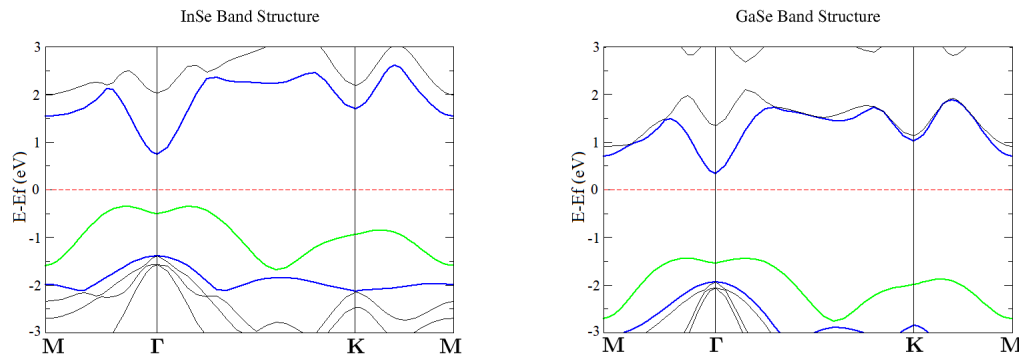


Figure 5.1: Band structure on InSe (on the left) and GaSe (on the right) in the form of monolayers.

noticed that GaSe presents features of its band structure that are similar to those of InSe: minimum of the CB in Γ , maximum of VB along the $\Gamma \rightarrow \mathbf{K}$ direction and the already mentioned sombrero-shaped dispersion around the point Γ (i.e. the presence of two maxima around that k-value and an almost flat VB between them). As previously mentioned this leads to the possibility for electrons to be easily transferred between energetically near states with a very small amount of thermal energy giving rise to an enhanced electronic transition probability between VB and CB. The two materials differ just for the values of their bandgaps: 1.24 eV for InSe and 1.88 eV in the case of GaSe. Although a cutoff of 45 Ry well satisfies our requirements for the study of the electronic properties of these two materials, it is not suitable for the next part of our analysis. In order to calculate an accurate phase diagram of the $\text{In}_{1-x}\text{Ga}_x\text{Se}$ alloy, indeed, the Cluster Expansion requires the generation and the study of a large number of structures. Each of them is composed by a number of atoms which is not known a priori and that can differ from the one of other structures, in addition atomic positions and In/Ga fractions can vary in a wide range of combinations. If we want to guarantee the accuracy and the carefulness of results, avoiding the use of misleading structures, it is therefore necessary to use a cutoff energy which well describes also the stress to which cells are subjected along each direction. In order to determine the more suited cutoff values, we have performed this test on the two primitive cells of InSe and GaSe for different cutoffs (from 40 to 100 Ry). According to results shown in figure 5.2, we

can say that 80 Ry represent a good compromise between the computational cost of the simulations and their accuracy. It is clear, indeed, that even with higher cutoffs the stress values remain almost constant meaning that higher E_{CutOff} does not provide any significant accuracy improvement. The Cluster Expansion method has been performed

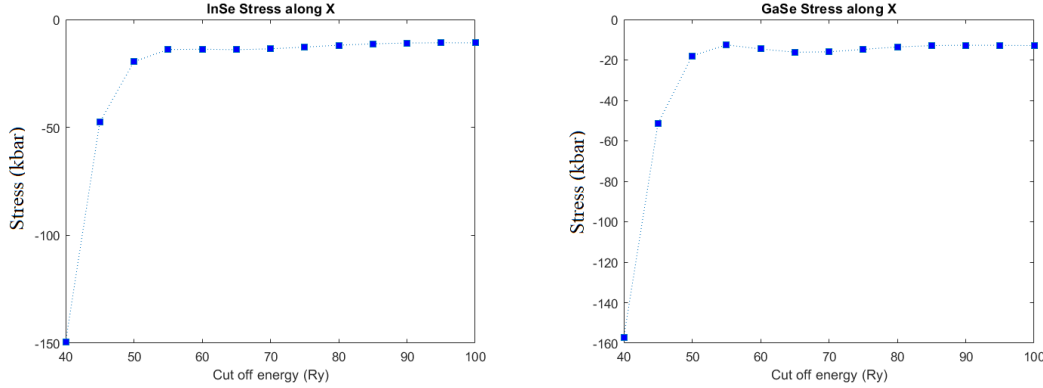


Figure 5.2: Stress values along the x direction (equal to the one along y) of the InSe and GaSe primitive cell as a function of the PW cutoff energies.

according to the theory explained in section 2.5 and, in particular, the process has been stopped when the value of the cross-validation score was equal to 0.00795 (well below $k_B T$). The obtained phase diagram is reported in figure 5.3. On the x axis the graph reports the Ga concentration in the alloy, i.e. $x=0$ corresponds to pure InSe while for $x=1$ we have pure GaSe. On the y axis the formation energies of the alloys are shown. These values were calculated through the following formula:

$$E_{FORM} = E_{Alloy} - [(1-x)\mu_{In} + x\mu_{Ga} + \mu_{Se}]$$

where x is the Ga concentration, E_{alloy} is the total energy of the corresponding alloy structure and μ_{In} , μ_{Ga} and μ_{Se} are the chemical potentials of In, Ga and Se, respectively, in their bulk phases. Green dots indicates energies of structures that have been calculated with the DFT method, while the blue crosses represent energies of the structures that have been predicted through the Cluster Expansion by exploiting equation 2.38. Red dots represent instead energies of the two ground states associated to the two pure phases, i.e. pure InSe and pure GaSe, and the red line which connects them predicts the ground-state energy for any In/Ga fraction. In order to estimate the accuracy of our results, we have compared the formation energies of the two pure phases with their formation enthalpy values which can be found in literature. For GaSe we have a reference value of -1.18 eV [82] which differs of $\approx 0.01 eV$ from our -1.17 eV while for what concerns InSe, our references indicate -1.01 eV [82] and -1.1 eV [112] that are very close to the value of -1.07 eV we have obtained. Variations from references are extremely small and the formation energy of GaSe is confirmed to be more negative than the one of InSe. By analysing the phase diagram, we are able to understand, for

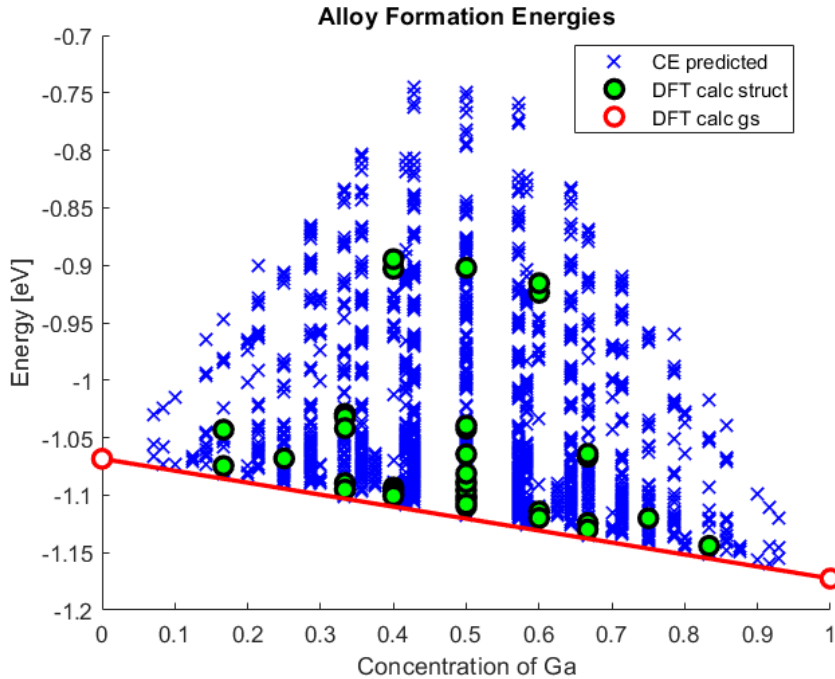


Figure 5.3: Predicted $In_{1-x}Ga_xSe$ alloy phase diagram . Blue crosses represent the energies of the structures predicted through the Cluster Expansion, green dots, instead, indicate the energies found with DFT calculations performed on generated structures and red dots represent instead energies of the two ground states associated to the two pure phases of InSe and GaSe respectively.

any concentration of Ga, which is the more stable structure, that is the one with a formation energy as close as possible to the one of the predicted ground state for that specific In/Ga fraction. In particular, according to data reported in figure 5.3 we have found the more stable systems for different concentrations and in the next section we have analysed their electronic properties. Interestingly the formation energies of the alloys varies linearly from the right side of the graph to the left side of the graph.

5.2 $In_{1-x}Ga_xSe$ electronic properties

According to the data obtained through the combination of Cluster Expansion and DFT methods we have predicted stable structures for different Ga concentrations, and selected some of them to perform an in depth analysis of the electronic properties of the alloys, in particular for $x=16.67\%$, 33.33% , 40% , 50% , 60% , 66.67% and 83.33% of Ga. We were interested, specifically, in the possibility to exploit InGaSe as single-photon emitter and for this reason we have studied its electronic properties in terms of band diagrams. From a practical point of view, the computational conditions were the same exploited in chapters 3 and 4 (i.e. cutoff energy of 45 Ry and number of

sampling k-points (2 2 1)). In figure 5.4 we have reported the graphs related to the two structures in which we have the lowest (on the left) and the highest (on the right) Ga concentrations, respectively. Looking at the two highlighted bands, we can notice that the two band structures resemble the band diagram on pure semiconductors without impurity defects. Furthermore, it is possible to notice that they are very similar to their counterpart in the two pure phases (i.e. pure InSe and pure GaSe) since they are characterized by the minimum of the conduction band placed in Γ and the maximum of the valence band located along the $\Gamma \rightarrow K$ path. In addition, the VB top most energy level shows two smooth hillocks around Γ , which give rise to an enhanced e^- transition probability through the bandgap, that remind us the characteristic sombrero-shaped dispersion present both in InSe and GaSe.

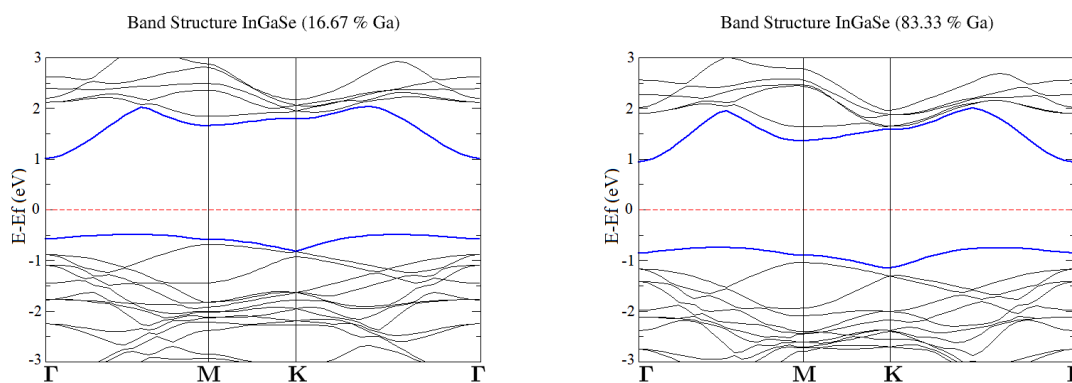


Figure 5.4: Band diagrams of the two structures at the extremes of our phase diagram: the one with $x=16.67\%$ of Ga, on the left, and the one where Ga concentration is $x=83.33\%$, on the right.

Focusing on the analysis of the bandgap values obtained by varying x , we notice that the band gap changes monotonically with the Gallium concentration, e.g. 1.24 eV, in the case with 0 % of Ga, to 1.88 eV where Ga concentration is 100 % (these are values of the direct bandgaps measured in Γ). This is an important result since it proves the possibility of tuning the bandgap of InSe by alloying with Ga; in particular it can be seen that the higher is the Ga concentration, the wider is the bandgap. Figure 5.5 shows the behaviour of the direct and indirect bandgaps of InGaSe while moving between the two pure phases of InSe and GaSe. We can notice a sudden change in their values for small percentages of Ga, while the increase becomes smoother at higher doping levels. The variation range is wide and offers promising possibilities of engineering bandgap value which, at least from a theoretical point of view, allow for InSe to emit photons in different regions of the electromagnetic spectrum.

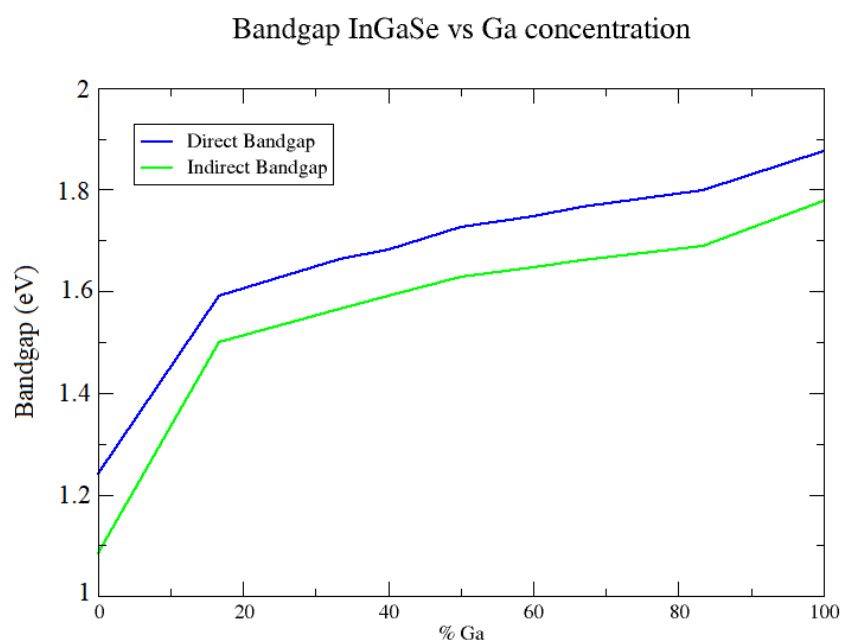


Figure 5.5: Direct and indirect bandgap behaviours of InGaSe as a function of the percentage of Ga in the alloy.

Conclusions

In the first part of this thesis work we have studied a monolayer of InSe and its applicability as SPE. The analysis of this material has been carried out using Density Functional Theory (DFT) simulations. Before investigating possible material modifications needed to obtain a single photon source, we determined the computational conditions which are needed to obtain accurate results. Through several tests we have hence evaluated the optimal cutoff energy of the basis wavefunctions, along with its associated equilibrium lattice parameter of InSe, the number of sampling k-points in the BZ and whether the spin orbit coupling was needful or not. We validated the accuracy of our results by comparing the predicted InSe band diagram with the one reported in several reference articles. Following, through DFT simulations we have studied many possible impurity defects to be embedded in the InSe bidimensional lattice and we have examined the electronic properties of all the resulting structures in terms of formation energies, band structures, density of states and spatial distributions of the molecular orbitals (MO) associated to the defects. The removal of a selenium atom (i.e. addition of a Se vacancy) from the monolayer and the substitutional impurity of a Se atom with one of Ge lead to the formation of well defined energy states within the bandgap: a donor level, in the case of the vacancy, and an acceptor one, in the case of the substitutional impurity. Both of these levels are extremely narrow and deep within the bandgap, thus they can be exploited to generate single photons; the donor level, in particular, is closer to the valence band, while the acceptor state is closer to the conduction band, offering the opportunity to the user to select the modification better suited for his own application. In addition we have studied substitutional impurities of Se with atoms belonging to the V group of the periodic table, especially nitrogen, phosphorous and arsenic. The resulting defect states, as well as in the two cases previously mentioned, are narrow and deep within the bandgap thus are suitable for the emission of single photons. Moreover, they show a double nature: they can work both as donor and as acceptor level offering even more degrees of freedom to the user. Formation energies of all above mentioned impurities are positive, thus none of them is thermodynamically favoured, however, they ranges from 1.69 eV (As in place of Se) to 2.95 eV (Ge in place of Se) that are not excessively high values. Our results are then technologically accessible and applicable, and demonstrate that the inclusion of V group atoms (i.e. N, P, As), Ge atoms or Se vacancy in the InSe matrix gives

rise to defects states that meet fundamental requirements of single photon emission, offering deep energy levels within the InSe bandgap and strong spatial localization. In the second part of this thesis work, we have studied the electronic properties of $In_{1-x}Ga_xSe$ alloy and its possible exploitation as SPE for different Ga concentrations. To this aim we employed the Cluster Expansion method combined with DFT calculation to predict its phase diagram which provides information about the more stable structures for any In/Ga fractions. Electronic properties of these structures have been then analyzed in terms of band diagrams. However, according to obtained data, it has been shown that this alloy is not suited to work as single photon source since it does not present Delta-like defects states within the bandgap. Nevertheless, we have found that its energy gap passes from 1.24 eV in the case with 0 % of Ga, to 1.88 eV where Ga concentration is 100 % and it increases monotonically in between; this offers the opportunity of tuning the InSe bandgap by alloying it with GaSe leading to the possibility of engineering the photon emission/absorption.

To conclude, our results highlight that some of the the proposed substitutional impurities in InSe are promising for single photon emission applications considering the depth and the localization of the defect level and thank to the possibility to tune the emission frequency. This work introduces new possibilities for employing quantum emitters in 2D materials for emerging applications, applications in nanophotonics and nanoscale sensing devices.

Bibliography

- [1] Frank Diedrich and Herbert Walther. Nonclassical radiation of a single stored ion. , 58(3):203–206, January 1987. doi: 10.1103/PhysRevLett.58.203.
- [2] Englund D. Toth M. Aharonovich, I. Solid-state single-photon emitters. *Nature Photon*, Sept 2016. doi: <https://doi.org/10.1038/nphoton.2016.186>.
- [3] Sonja; Zarda Patrick; Weinfurter Harald Kurtsiefer, Christian; Mayer. Stable solid- state source of single photons. *Phys. Rev. Lett.*, 85(2):290–293, 2000.
- [4] Robert H. Hadfield. Single-photon detectors for optical quantum information applications. *Nature Photonics*, 3(12):696–705, December 2009. doi: 10.1038/nphoton.2009.230.
- [5] Mark Oxborrow and Alastair G Sinclair. Single-photon sources. *Contemporary Physics*, 46(3):173–206, 2005. doi: 10.1080/00107510512331337936. URL <https://doi.org/10.1080/00107510512331337936>.
- [6] Stefan Scheel. Single-photon sources—an introduction. *Journal of Modern Optics*, 56(2-3):141–160, 2009. doi: 10.1080/09500340802331849. URL <https://doi.org/10.1080/09500340802331849>.
- [7] M. D. Eisaman, J. Fan, A. Migdall, and S. V. Polyakov. Invited review article: Single-photon sources and detectors. *Review of Scientific Instruments*, 82(7):071101, 2011. doi: 10.1063/1.3610677. URL <https://doi.org/10.1063/1.3610677>.
- [8] Sergey Polyakov, Alan Migdall, Jingyun Fan, and J. Bienfang. *Single-Photon Generation and Detection*. 12 2013. ISBN 978-0123876959.
- [9] Christopher J. Chunnillall, Ivo Pietro Degiovanni, Stefan Kück, Ingmar Müller, and Alastair G. Sinclair. Metrology of single-photon sources and detectors: a review. *Optical Engineering*, 53(8):1 – 17, 2014. doi: 10.1117/1.OE.53.8.081910. URL <https://doi.org/10.1117/1.OE.53.8.081910>.

- [10] White A, Senellart P, Solomon G. High-performance semiconductor quantum-dot single-photon sources. *Nat. Nanotechnol.*, 2017. doi: 10.1038/nnano.2017.218.PMID:29109549.
- [11] Fulvio Flamini, Nicolò Spagnolo, and Fabio Sciarrino. Photonic quantum information processing: a review. *Reports on Progress in Physics*, 82(1):016001, nov 2018. doi: francesca11. URL <https://doi.org/10.1088%2F1361-6633%2Faad5b2>.
- [12] Lucia Caspani, Chunle Xiong, Benjamin J. Eggleton, Daniele Bajoni, Marco Liscidini, Matteo Galli, Roberto Morandotti, and David J. Moss. Integrated sources of photon quantum states based on nonlinear optics. *Light: Science & Applications*, 6, November 2017. URL <https://strathprints.strath.ac.uk/61166/>.
- [13] Paul Adrien Maurice Dirac and Niels Henrik David Bohr. The quantum theory of the emission and absorption of radiation. *Proceedings of the Royal Society of London. Series A, Containing Papers of a Mathematical and Physical Character*, 114(767):243–265, 1927. doi: 10.1098/rspa.1927.0039. URL <https://royalsocietypublishing.org/doi/abs/10.1098/rspa.1927.0039>.
- [14] H. J. Kimble, M. Dagenais, and L. Mandel. Photon antibunching in resonance fluorescence. *Phys. Rev. Lett.*, 39:691–695, Sep 1977. doi: 10.1103/PhysRevLett.39.691. URL <https://link.aps.org/doi/10.1103/PhysRevLett.39.691>.
- [15] Evan Meyer-Scott, Christine Silberhorn, and Alan Migdall. Single-photon sources: Approaching the ideal through multiplexing. *Review of Scientific Instruments*, 91(4):041101, 2020. doi: 10.1063/5.0003320. URL <https://doi.org/10.1063/5.0003320>.
- [16] Roy Glauber. The quantum theory of optical coherence. *Phys. Rev.*, 130:2529, 06 1963. doi: 10.1103/PhysRev.130.2529.
- [17] TWISS R. BROWN, R. Correlation between photons in two coherent beams of light. *Nature*, January 1956. doi: <https://doi.org/10.1038/177027a0>.
- [18] TWISS R. HANBURY BROWN, R. A test of a new type of stellar interferometer on sirius. *Nature*, November 1956. doi: <https://doi.org/10.1038/1781046a0>.
- [19] Aspuru-Guzik A and Walther P. Photonic quantum simulators. *Nature Physics*, 2012. doi: 10.1038/nphys2253. URL <https://doi.org/10.1038/nphys2253>.
- [20] Peter Lodahl, Sahand Mahmoodian, and Søren Stobbe. Interfacing single photons and single quantum dots with photonic nanostructures. *Rev. Mod. Phys.*, 87: 347–400, May 2015. doi: 10.1103/RevModPhys.87.347. URL <https://link.aps.org/doi/10.1103/RevModPhys.87.347>.

- [21] Nick Vamivakas Chitraleema Chakraborty and Dirk Englund. Advances in quantum light emission from 2d materials. *Nanophotonics*, 8, 2019. doi: <https://doi.org/10.1515/nanoph-2019-0140>.
- [22] URL <https://meshb.nlm.nih.gov/record/ui?name=SPECT>.
- [23] Curty M. Lo H.K. and Tamaki K. Secure quantum key distribution. *Nature Physics*, 2014. doi: 10.1038/nphoton.2014.149. URL <https://www.nature.com/articles/nphoton.2014.149>.
- [24] Brahim Lounis and Michel Orrit. Single-photon sources. *Reports on Progress in Physics*, 68(5):1129–1179, apr 2005. doi: 10.1088/0034-4885/68/5/r04. URL <https://doi.org/10.1088%2F0034-4885%2F68%2F5%2Fr04>.
- [25] Gillen J. Peng A. et al. Bakr, W. A quantum gas microscope for detecting single atoms in a hubbard-regime optical lattice. 11 2009. doi: <https://doi.org/10.1038/nature08482>.
- [26] Pollet L. Gerbier F. et al. Trotzky, S. Suppression of the critical temperature for superfluidity near the mott transition. 10 2010. doi: <https://doi.org/10.1038/nphys1799>.
- [27] Endres M. Sherson J. et al. Weitenberg, C. Single-spin addressing in an atomic mott insulator. 03 2011. doi: <https://doi.org/10.1038/nature09827>.
- [28] Maciej Lewenstein, Anna Sanpera, Veronica Ahufinger, Bogdan Damski, Aditi Sen(De), and Ujjwal Sen. Ultracold atomic gases in optical lattices: mimicking condensed matter physics and beyond. *Advances in Physics*, 56(2):243–379, 2007. doi: 10.1080/00018730701223200. URL <https://doi.org/10.1080/00018730701223200>.
- [29] Schmitz H. Glueckert J. et al Friedenauer, A. Simulating a quantum magnet with trapped ions. *Nature Phys*, 07 2008. doi: <https://doi.org/10.1038/nphys1032>.
- [30] Kirchmair G. Zähringer F. et al. Gerritsma, R. Quantum simulation of the dirac equation. *Nature*, 01 2010. doi: <https://doi.org/10.1038/nature08688>.
- [31] Müller M. Schindler P. et al. Barreiro, J. An open-system quantum simulator with trapped ions. *Nature*, 02 2011. doi: <https://doi.org/10.1038/nature09801>.
- [32] Edwards E. Kim K. et al. Islam, R. Onset of a quantum phase transition with a trapped ion quantum simulator. *Nat Commun*, 07 2011. doi: <https://doi.org/10.1038/ncomms1374>.

- [33] Chang M. Korenblit S. et al. Kim, K. Quantum simulation of frustrated ising spins with trapped ions. *Nature*, 06 2010. doi: <https://doi.org/10.1038/nature09071>.
- [34] Roos C. Blatt, R. Quantum simulations with trapped ions. *Nature Phys*, 04 2012. doi: <https://doi.org/10.1038/nphys2252>.
- [35] Peter J. Love Martin Head-Gordon Alán Aspuru-Guzik, Anthony D. Dutoi. Simulated quantum computation of molecular energies. *Science*. doi: 10.1126/science.1113479.
- [36] Seth Lloyd Daniel S. Abrams. Simulation of many-body fermi systems on a universal quantum computer. *Phys.Rev.Lett.* 79 (1997) 2586-2589, . doi: 10.1103/PhysRevLett.79.2586.
- [37] Seth Lloyd Daniel S. Abrams. A quantum algorithm providing exponential speed increase for finding eigenvalues and eigenvectors. *Phys.Rev.Lett.* 83:5162-5165, 1999, . doi: 10.1103/PhysRevLett.83.5162.
- [38] Whitfield J. Gillett G. et al. Lanyon, B. Towards quantum chemistry on a quantum computer. 2010. doi: <https://doi.org/10.1038/nchem.483>.
- [39] Alán Aspuru-Guzik, Anthony D. Dutoi, Peter J. Love, and Martin Head-Gordon. Simulated quantum computation of molecular energies. *Science*, 309(5741):1704–1707, 2005. ISSN 0036-8075. doi: 10.1126/science.1113479. URL <https://science.sciencemag.org/content/309/5741/1704>.
- [40] A. Yu. Kitaev. Quantum measurements and the abelian stabilizer problem, 1995.
- [41] Guifré Vidal. Efficient classical simulation of slightly entangled quantum computations. *Physical Review Letters*, 91(14), Oct 2003. ISSN 1079-7114. doi: 10.1103/physrevlett.91.147902. URL <http://dx.doi.org/10.1103/PhysRevLett.91.147902>.
- [42] Politi A. Stefanov A. et al. Matthews, J. Manipulation of multiphoton entanglement in waveguide quantum circuits. *Nature Photon*, 05 2009. doi: <https://doi.org/10.1038/nphoton.2009.93>.
- [43] Raffaele Santagati, Jianwei Wang, Antonio Andrea Gentile, Stefano Paesani, Nathan Wiebe, Jarrod McClean, Sam Morley-Short, Peter Shadbolt, Damien Bonneau, Joshua Silverstone, David Tew, Xiaoqi Zhou, Jeremy O'Brien, and Mark Thompson. Witnessing eigenstates for quantum simulation of hamiltonian spectra. *Science Advances*, 4:eaap9646, 01 2018. doi: 10.1126/sciadv.aap9646.
- [44] URL <http://www.prweb.com/releases/2009/tucson/prweb2737304.htm>.

- [45] Igor Aharonovich, Chunyuan Zhou, Alastair Stacey, Julius Orwa, Stefania Castelletto, David Simpson, Andrew D. Greentree, François Treussart, Jean-François Roch, and Steven Praver. Enhanced single-photon emission in the near infrared from a diamond color center. *Phys. Rev. B*, 79:235316, Jun 2009. doi: 10.1103/PhysRevB.79.235316. URL <https://link.aps.org/doi/10.1103/PhysRevB.79.235316>.
- [46] Hartmann N. Baldwin J. et al. Ma, X. Room-temperature single-photon generation from solitary dopants of carbon nanotubes. *Nature Nanotech.* doi: <https://doi.org/10.1038/nnano.2015.136>.
- [47] Igor Aharonovich and Elke Neu. Diamond nanophotonics. *Advanced Optical Materials*, 2(10):911–928, 2014. doi: 10.1002/adom.201400189. URL <https://onlinelibrary.wiley.com/doi/abs/10.1002/adom.201400189>.
- [48] A. Sipahigil, K. D. Jahnke, L. J. Rogers, T. Teraji, J. Isoya, A. S. Zibrov, F. Jelezko, and M. D. Lukin. Indistinguishable photons from separated silicon-vacancy centers in diamond. *Phys. Rev. Lett.*, 113:113602, Sep 2014. doi: 10.1103/PhysRevLett.113.113602. URL <https://link.aps.org/doi/10.1103/PhysRevLett.113.113602>.
- [49] Moon H. Lienhard B. et al. Grosso, G. Tunable and high-purity room temperature single-photon emission from atomic defects in hexagonal boron nitride. *Nature Communications*. doi: <https://doi.org/10.1038/s41467-017-00810-2>.
- [50] Dan Dalacu, Philip J Poole, and Robin L Williams. Nanowire-based sources of non-classical light. *Nanotechnology*, 30(23):232001, mar 2019. doi: 10.1088/1361-6528/ab0393. URL <https://doi.org/10.1088%2F1361-6528%2Fab0393>.
- [51] J. Hours, S. Varoutsis, M. Gallart, J. Bloch, I. Robert-Philip, A. Cavanna, I. Abram, F. Laruelle, and J. M. Gérard. Single photon emission from individual GaAs quantum dots. *Applied Physics Letters*, 82(14):2206–2208, 2003. doi: 10.1063/1.1563050. URL <https://doi.org/10.1063/1.1563050>.
- [52] Belyaev K.G. Klimko G.V. et al. Rakhlin, M.V. Tinas/algaas quantum dots for single-photon emission in a red spectral range. *Sci Rep.* doi: <https://doi.org/10.1038/s41598-018-23687-7>.
- [53] The Editors of Encyclopaedia Britannica. Colour centre. URL <https://www.britannica.com/science/color-center>.
- [54] Ariful Haque and Sharaf Sumaiya. An overview on the formation and processing of nitrogen-vacancy photonic centers in diamond by ion implantation. *Journal of Manufacturing and Materials Processing*, 1(1), 2017. ISSN 2504-4494. doi: 10.3390/jmmp1010006. URL <https://www.mdpi.com/2504-4494/1/1/6>.

- [55] Gabriella D Shepard, Obafunso A Ajayi, Xiangzhi Li, X-Y Zhu, James Hone, and Stefan Strauf. Nanobubble induced formation of quantum emitters in monolayer semiconductors. *2D Materials*, 4(2):021019, mar 2017. doi: article333.23. URL <https://doi.org/10.1088%2F2053-1583%2Faa629d>.
- [56] Romain Bourrellier, Sophie Meuret, Anna Tararan, Odile Stéphan, Mathieu Kociak, Luiz H. G. Tizei, and Alberto Zobelli. Bright uv single photon emission at point defects in h-bn. *Nano Letters*, 16(7):4317–4321, 2016. doi: 10.1021/acs.nanolett.6b01368. URL <https://doi.org/10.1021/acs.nanolett.6b01368>.
- [57] Nicholas McDougall, Jim Partridge, Rebecca Nicholls, Salvy Russo, and D.G McCulloch. Influence of point defects on the near edge structure of hexagonal boron nitride. *Physical Review B*, 96, 10 2017. doi: 10.1103/PhysRevB.96.144106.
- [58] A. Katzir, J. T. Suss, A. Zunger, and A. Halperin. Point defects in hexagonal boron nitride. I. EPR, thermoluminescence, and thermally-stimulated-current measurements. , 11(6):2370–2377, March 1975. doi: 10.1103/PhysRevB.11.2370.
- [59] T. Taniguchi and K. Watanabe. Synthesis of high-purity boron nitride single crystals under high pressure by using ba–bn solvent. *Journal of Crystal Growth*, 303(2):525 – 529, 2007. ISSN 0022-0248. doi: <https://doi.org/10.1016/j.jcrysgro.2006.12.061>. URL <http://www.sciencedirect.com/science/article/pii/S0022024807000486>.
- [60] X. Z. Du, J. Li, J. Y. Lin, and H. X. Jiang. The origin of deep-level impurity transitions in hexagonal boron nitride. *Applied Physics Letters*, 106(2):021110, 2015. doi: 10.1063/1.4905908. URL <https://doi.org/10.1063/1.4905908>.
- [61] Luc Museur, Demetrios Anglos, Jean-Pierre Petitet, Jean-Pierre Michel, and Andrei V. Kanaev. Photoluminescence of hexagonal boron nitride: Effect of surface oxidation under uv-laser irradiation. *Journal of Luminescence*, 127(2):595 – 600, 2007. ISSN 0022-2313. doi: <https://doi.org/10.1016/j.jlumin.2007.01.024>. URL <http://www.sciencedirect.com/science/article/pii/S0022231307001172>.
- [62] Muhammad Safwan Zaini. What is meant by bohr exciton radius and what is the role in quantum confinement effect? 07 2019.
- [63] V. Smejkal J. Burgdörfer T. Mueller F. Libisch L. Linhart, M. Paur. Localized inter-valley defect excitons as single-photon emitters in wse_2 . *Phys. Rev. Lett.* doi: 10.1103/PhysRevLett.123.146401.
- [64] Yu Li Huang Pranjali Kumar Gogoi Ming Yang Li Lain-Jong Li Paolo E. Trevisanutto Qixing Wang Stephen J Pennycook Andrew Thye Shen Wee Su Ying Quek Yu Jie Zheng, Yifeng Chen. Point defects and localized excitons in 2d wse_2 . doi: 10.1021/acsnano.9b02316.

- [65] A Sajid, Michael J Ford, and Jeffrey R Reimers. Single-photon emitters in hexagonal boron nitride: a review of progress. *Reports on Progress in Physics*, 83(4): 044501, mar 2020. doi: 10.1088/1361-6633/ab6310. URL <https://doi.org/10.1088%2F1361-6633%2Fab6310>.
- [66] Andrew D Greentree, Paolo Olivero, Martin Draganski, Elizabeth Trajkov, James R Rabeau, Patrick Reichart, Brant C Gibson, Sergey Rubanov, Shane T Huntington, David N Jamieson, and Steven Prawer. Critical components for diamond-based quantum coherent devices. *Journal of Physics: Condensed Matter*, 18(21):S825–S842, may 2006. doi: 10.1088/0953-8984/18/21/s09. URL <https://doi.org/10.1088%2F0953-8984%2F18%2F21%2Fs09>.
- [67] L. Debbichi, O. Eriksson, and S. Lebègue. Two-dimensional indium selenides compounds: An ab initio study. *The Journal of Physical Chemistry Letters*, 6(15):3098–3103, 2015. doi: 10.1021/acs.jpcllett.5b01356. URL <https://doi.org/10.1021/acs.jpcllett.5b01356>. PMID: 26267208.
- [68] Barker A Andrei E.Y. Du X, Skachko I. Approaching ballistic transport in suspended graphene. *Nat Nano*, 2008. doi: 10.1038/nnano.2008.199.
- [69] Lin Y.M. Valdes-Garcia A Avouris P Xia F.N., Mueller T. Ultrafast graphene photodetector. *Nat Nano*, 2009. doi: 10.1038/nnano.2009.292.
- [70] Juan Francisco Sánchez Royo, Guillermo Muñoz-Matutano, Mauro Brotons-Gisbert, J. Martinez-Pastor, Alfredo Segura, Andres Cantarero, R. Mata, Josep Canet-Ferrer, Gerard Tobias, Enric Canadell, Jose Marques-Hueso, and Brian Gerardot. Electronic structure, optical properties, and lattice dynamics in atomically thin indium selenide flakes. *Nano Research*, 7:1556, 08 2014. doi: 10.1007/s12274-014-0516-x.
- [71] Qiu M Cao R Guo Z Zhao J Li Y Xiao Q Fan D Zhang H Sang DK, Wang H. Two dimensional β -inse with layer-dependent properties: Band alignment, work function and optical properties. *Nanomaterials (Basel)*, 9, 01 2019. doi: 10.3390/nano9010082.
- [72] Ali Eftekhari. Tungsten dichalcogenides (ws2, wse2, and wte2): materials chemistry and applications. *J. Mater. Chem. A*, 5:18299–18325, 2017. doi: 10.1039/C7TA04268J. URL <http://dx.doi.org/10.1039/C7TA04268J>.
- [73] Ali Kandemir and Hasan Sahin. Janus single layers of in 2 sse : A first-principles study. *Physical Review B*, 97, 04 2018. doi: 10.1103/PhysRevB.97.155410.
- [74] Shan J. Mak K. Photonics and optoelectronics of 2d semiconductor transition metal dichalcogenides. *Nature Photon*, 2016. doi: <https://doi.org/10.1038/nphoton.2015.282>.

- [75] Xiang-Xiang Song, Di Liu, Vahid Mosallanejad, Jie You, Tian-Yi Han, Dian-Teng Chen, Hai-Ou Li, Gang Cao, Ming Xiao, Guang-Can Guo, and Guo-Ping Guo. A gate defined quantum dot on the two-dimensional transition metal dichalcogenide semiconductor wse₂. *Nanoscale*, 7:16867–16873, 2015. doi: 10.1039/C5NR04961J. URL <http://dx.doi.org/10.1039/C5NR04961J>.
- [76] Matthew Brooks and Guido Burkard. Theory of strain-induced confinement in transition metal dichalcogenide monolayers. *Phys. Rev. B*, 97(19):195454, May 2018. doi: 10.1103/PhysRevB.97.195454.
- [77] David G. Hopkinson, Viktor Zólyomi, Aidan P. Rooney, Nick Clark, Daniel J. Terry, Matthew Hamer, David J. Lewis, Christopher S. Allen, Angus I. Kirkland, Yuri Andreev, Zakhar Kudrynskyi, Zakhar Kovalyuk, Amalia Patanè, Vladimir I. Fal’ko, Roman Gorbachev, and Sarah J. Haigh. Formation and healing of defects in atomically thin gase and inse. *ACS Nano*, 13(5):5112–5123, 2019. doi: 10.1021/acsnano.8b08253. URL <https://doi.org/10.1021/acsnano.8b08253>.
- [78] Himani Arora, Younghun Jung, Tommaso Venanzi, Kenji Watanabe, Takashi Taniguchi, René Hübner, Harald Schneider, Manfred Helm, James C. Hone, and Artur Erbe. Effective hexagonal boron nitride passivation of few-layered inse and gase to enhance their electronic and optical properties. *ACS Applied Materials & Interfaces*, 11(46):43480–43487, 2019. doi: 10.1021/acсами.9b13442. URL <https://doi.org/10.1021/acсами.9b13442>.
- [79] P. Gomes da Costa, R. G. Dandrea, R. F. Wallis, and M. Balkanski. First-principles study of the electronic structure of γ -inse and β -inse. *Phys. Rev. B*, 48:14135–14141, Nov 1993. doi: 10.1103/PhysRevB.48.14135. URL <https://link.aps.org/doi/10.1103/PhysRevB.48.14135>.
- [80] Xueping Li, Juan Du, Wenqi Xiong, and Congxin Xia. Impurity states in inse monolayers doped with group ii and iv elements. *Journal of Applied Physics*, 122(18):185702, 2017. doi: 10.1063/1.4998326. URL <https://doi.org/10.1063/1.4998326>.
- [81] Alfredo Segura. Layered indium selenide under high pressure: A review. doi: <https://doi.org/10.3390/cryst8050206>.
- [82] Anubhav Jain, Shyue Ping Ong, Geoffroy Hautier, Wei Chen, William Davidson Richards, Stephen Dacek, Shreyas Cholia, Dan Gunter, David Skinner, Gerbrand Ceder, and Kristin a. Persson. The Materials Project: A materials genome approach to accelerating materials innovation. *APL Materials*, 1(1):011002, 2013. ISSN 2166532X. doi: 10.1063/1.4812323. URL <http://link.aip.org/link/AMPADS/v1/i1/p011002/s1&Agg=doi>.

- [83] Yu Geliang L. Mishchenko Artem Zólyomi Viktor Morozov Sergey V. Kumar Roshan Krishna Gorbachev Roman V. Kudrynskyi Zakhar R. Pezzini Sergio Kovalyuk Zakhar D. Zeitler Uli Novoselov Konstantin S. Patané Amalia Eaves Lawrence Grigorieva Irina V. Fal'ko Vladimir I. Geim Andre K. Cao Yang Bandurin Denis A., Tyurnina Anastasia V. High electron mobility, quantum hall effect and anomalous optical response in atomically thin inse. *Nature Nanotechnology*, 2017. doi: 10.1038/nnano.2016.242. URL <https://doi.org/10.1038/nnano.2016.242>.
- [84] Galli G Spanu L, Sorella S. Nature and strength of interlayer binding in graphite. *Phys. Rev. Lett.*, Nov 2009. doi: 10.1103/PhysRevLett.103.196401. URL <https://pubmed.ncbi.nlm.nih.gov/20365938>.
- [85] Jacobson N et al. Rydberg H, Dion M. Van der waals density functional for layered structures. *Phys. Rev. Lett.*, Sept 2003. doi: 10.1103/PhysRevLett.91.126402. URL <https://pubmed.ncbi.nlm.nih.gov/14525379>.
- [86] Jiadong Zhou, Jia Shi, Qingsheng Zeng, Yu Chen, Lin Niu, Fucui Liu, Ting Yu, Kazu Suenaga, Xinfeng Liu, Junhao Lin, and Zheng Liu. InSe monolayer: synthesis, structure and ultra-high second-harmonic generation. *2D Materials*, 5 (2):025019, mar 2018. doi: 10.1088/2053-1583/aab390. URL <https://doi.org/10.1088%2F2053-1583%2Faab390>.
- [87] Xi Chen, Zheng-Zhe Lin, and Ming Ju. Controllable band alignment transition in inse-mos2 van der waals heterostructure. *physica status solidi (RRL) – Rapid Research Letters*, 12(7):1800102, 2018. doi: 10.1002/pssr.201800102. URL <https://onlinelibrary.wiley.com/doi/abs/10.1002/pssr.201800102>.
- [88] P. Hohenberg and W. Kohn. Inhomogeneous electron gas. *Phys. Rev.*, 136: B864–B871, Nov 1964.
- [89] W. Kohn and L. J. Sham. Self-consistent equations including exchange and correlation effects. *Phys. Rev.*, 140:A1133–A1138, Nov 1965.
- [90] E. Fermi. Un metodo statistico per la determinazione di alcune prioriet  dell'atome. *Rend. Accad. Naz. Lincei*, 6:602, 1927.
- [91] L. H. Thomas. The calculation of atomic fields. *Proc. Cambridge Phil. Roy. Soc.*, 23:542, 1927.
- [92] P. A. M. Dirac. Note on exchange phenomena in the thomas-fermi atom. *Proc. Cambridge Phil. Roy. Soc.*, 26:376, 1930.
- [93] John P. Perdew and Karla Schmidt. Jacob's ladder of density functional approximations for the exchange-correlation energy. *AIP Conference Proceedings*,

- 577(1):1–20, 2001. doi: 10.1063/1.1390175. URL <http://link.aip.org/link/?APC/577/1/1>.
- [94] D. M. Ceperley and B. J. Alder. Ground state of the electron gas by a stochastic method. *Phys. Rev. Lett.*, 45:566–569, Aug 1980.
- [95] J. P. Perdew and Alex Zunger. Self-interaction correction to density-functional approximations for many-electron systems. *Phys. Rev. B*, 23:5048–5079, May 1981.
- [96] John P. Perdew and Wang Yue. Accurate and simple density functional for the electronic exchange energy: Generalized gradient approximation. *Phys. Rev. B*, 33:8800–8802, Jun 1986.
- [97] J. P. Perdew, K. Burke, and M. Ernzerhof. Generalized gradient approximation made simple. *Phys. Rev. Lett.*, 77:3865–3868, Oct 1996. doi: 10.1103/PhysRevLett.77.3865. URL <http://link.aps.org/%doi/10.1103/PhysRevLett.77.3865>.
- [98] H Hellmann. *Einführung in die quantumchemie*. 1937.
- [99] R. P. Feynman. Force in molecules. *Phys. Rev.*, 56:340–343, 1939.
- [100] James C. Phillips and Leonard Kleinman. New method for calculating wave functions in crystals and molecules. *Phys. Rev.*, 116:287–294, Oct 1959.
- [101] D. Vanderbilt. Soft self-consistent pseudopotentials in a generalized eigenvalue formalism. *Phys. Rev. B.*, 41:7892–7895, 1990.
- [102] Hendrik J. Monkhorst and James D. Pack. Special points for brillouin-zone integrations. *Phys. Rev. B*, 13:5188–5192, Jun 1976.
- [103] URL <https://publish.illinois.edu/atomicsscale/cluster-expansion/>.
- [104] B. Bieniek G. Hart, C. Rosenbrock and V. Blum. Hands-on tutorial on cluster expansion. July 2014. URL http://helper.ipam.ucla.edu/publications/gss2014/gss2014_12176.pdf.
- [105] J. W. D. Connolly and A. R. Williams. Density-functional theory applied to phase transformations in transition-metal alloys. *Phys. Rev. B*, 27:5169–5172, Apr 1983. doi: 10.1103/PhysRevB.27.5169. URL <https://link.aps.org/doi/10.1103/PhysRevB.27.5169>.
- [106] Xu Zhou, Jingxin Cheng, Yubing Zhou, Ting Cao, Hao Hong, Zhimin Liao, Shiwei Wu, Hailin Peng, Kaihui Liu, and Dapeng Yu. Strong second-harmonic generation in atomic layered gase. *Journal of the American Chemical Society*,

- 137(25):7994–7997, 2015. doi: 10.1021/jacs.5b04305. URL <https://doi.org/10.1021/jacs.5b04305>. PMID: 26060875.
- [107] Philipp Tonndorf, Stefan Schwarz, Johannes Kern, Iris Niehues, Osvaldo Del Pozo-Zamudio, Alexander I Dmitriev, Anatoly P Bakhtinov, Dmitry N Borisenko, Nikolai N Kolesnikov, Alexander I Tartakovskii, Steffen Michaelis de Vasconcellos, and Rudolf Bratschitsch. Single-photon emitters in GaSe. *2D Materials*, 4(2):021010, feb 2017. doi: 10.1088/2053-1583/aa525b. URL <https://doi.org/10.1088/2053-1583/aa525b>.
- [108] Nilanthy Balakrishnan, Zakhar R Kudrynskyi, Emily F Smith, Michael W Fay, Oleg Makarovsky, Zakhar D Kovalyuk, Laurence Eaves, Peter H Beton, and Amalia Patanè. Engineering p – n junctions and bandgap tuning of InSe nanolayers by controlled oxidation. *2D Materials*, 4(2):025043, mar 2017. doi: 10.1088/2053-1583/aa61e0. URL <https://doi.org/10.1088/2053-1583/aa61e0>.
- [109] Tyurnina A. Yu G. et al. Bandurin, D. High electron mobility, quantum hall effect and anomalous optical response in atomically thin inse. *Nature Nanotech*, Nov 2016. doi: <https://doi.org/10.1038/nnano.2016.242>.
- [110] Yang Li, Tianmeng Wang, Meng Wu, Ting Cao, Yanwen Chen, Raman Sankar, Rajesh K Ulaganathan, Fangcheng Chou, Christian Wetzel, Cheng-Yan Xu, Steven G Louie, and Su-Fei Shi. Ultrasensitive tunability of the direct bandgap of 2d InSe flakes via strain engineering. *2D Materials*, 5(2):021002, jan 2018. doi: 10.1088/2053-1583/aaa6eb. URL <https://doi.org/10.1088/2053-1583/aaa6eb>.
- [111] Sidong Lei, Liehui Ge, Sina Najmaei, Antony George, Rajesh Kappera, Jun Lou, Manish Chhowalla, Hisato Yamaguchi, Gautam Gupta, Robert Vajtai, Aditya D. Mohite, and Pulickel M. Ajayan. Evolution of the electronic band structure and efficient photo-detection in atomic layers of inse. *ACS Nano*, 8(2):1263–1272, 2014. doi: 10.1021/nn405036u. URL <https://doi.org/10.1021/nn405036u>. PMID: 24392873.
- [112] A. Krost F. Lévy S.F. Marenkin W. Richter N. Ringelstein R. Schmechel G. Weiser H. Weheit M. Yao W. Żdanowicz R. Clasen, P. Grosse. Non-tetrahedrally bonded elements and binary compounds i. 41C, 1998.